

1 **Deep manifold learning reveals hidden dynamics of**
2 **proteasome autoregulation**

3

4 **Zhaolong Wu¹, Shuwen Zhang^{1,2}, Wei Li Wang^{1,3,4}, Yinping Ma¹, Yuanchen Dong⁵ &**
5 **Youdong Mao^{1-4*}**

6 ¹State Key Laboratory for Mesoscopic Physics, School of Physics, Peking University, Beijing,

7 China. ²Center for Quantitative Biology, Peking University, Beijing, China. ³Intel Parallel

8 Computing Center for Structural Biology, Dana-Farber Cancer Institute, Boston, MA, USA.

9 ⁴Department of Cancer Immunology and Virology, Dana-Farber Cancer Institute, Department of

10 Microbiology, Harvard Medical School, Boston, MA, USA. ⁵Institute of Chemistry, Chinese

11 Academy of Sciences, Beijing, China.

12 *To whom correspondence may be addressed.

13

14 **Abstract**

15 **The 2.5-MDa 26S proteasome maintains proteostasis and regulates myriad cellular
16 processes¹. How polyubiquitylated substrate interactions regulate proteasome activity is
17 not understood^{1,2}. Here we introduce a deep manifold learning framework, named
18 AlphaCryo4D, which enables atomic-level cryogenic electron microscopy (cryo-EM)
19 reconstructions of nonequilibrium conformational continuum and reconstitutes ‘hidden’
20 dynamics of proteasome autoregulation in the act of substrate degradation. AlphaCryo4D
21 integrates 3D deep residual learning³ with manifold embedding⁴ of free-energy landscapes⁵,
22 which directs 3D clustering via an energy-based particle-voting algorithm. In blind
23 assessments using simulated heterogeneous cryo-EM datasets, AlphaCryo4D achieved 3D
24 classification accuracy three times that of conventional methods⁶⁻⁹ and reconstructed
25 continuous conformational changes of a 130-kDa protein at sub-3-Å resolution. By using
26 AlphaCryo4D to analyze a single experimental cryo-EM dataset², we identified 64
27 conformers of the substrate-bound human 26S proteasome, revealing conformational
28 entanglement of two regulatory particles in the doubly capped holoenzymes and their
29 energetic differences with singly capped ones. Novel ubiquitin-binding sites are discovered
30 on the RPN2, RPN10 and α 5 subunits to remodel polyubiquitin chains for deubiquitylation
31 and recycle. Importantly, AlphaCryo4D choreographs single-nucleotide-exchange
32 dynamics of proteasomal AAA-ATPase motor during translocation initiation, which
33 upregulates proteolytic activity by allosterically promoting nucleophilic attack. Our
34 systemic analysis illuminates a grand hierarchical allostery for proteasome autoregulation.**

35

36

37 The 26S proteasome is the known largest ATP-dependent protease machinery of ~2.5 MDa
38 molecular weight ubiquitously found in all eukaryotic cells. It exists at the center of the
39 ubiquitin-proteasome system (UPS) that regulates myriad cellular processes, such as protein
40 quality control, cell cycle, gene expression, inflammation and immunity^{1,2}. Dysregulation of the
41 UPS has been broadly associated with carcinogenesis, ageing, neurodegenerative and
42 cardiovascular diseases¹. The 26S holoenzyme is assembled by a cylindrical 20S core particle
43 (CP) capped with one or two 19S regulatory particles (RPs), each consisting of the lid and base
44 subcomplexes^{1,2}. The ring-like heterohexameric motor of ATPases-associated-with-diverse-
45 cellular-activities (AAA) ATPase in the base subcomplex mechanically unfold polyubiquitylated
46 substrates recognized by ubiquitin receptors in the lid subcomplex. Previous structural data by
47 cryogenic electron microscopy (cryo-EM) have suggested three modes of coordinated ATP
48 hydrolysis in the AAA-ATPase motor that regulate distinct steps of ubiquitin recognition,
49 deubiquitylation, initiation of translocation and processive substrate translocation in the
50 proteasome². However, key intermediate conformations between these states were missing,
51 greatly limiting our understanding of the intrinsic proteasome regulation. The mechanism of the
52 proteasome targeting of substrate-conjugated ubiquitin signals is not fully understood^{1,10-12}. How
53 polyubiquitylated substrate interactions regulate proteasome activity remains enigmatic¹.

54 The 26S proteasome is one of the most complex, dynamic and conformationally
55 heterogeneous holoenzyme machinery in cells^{2,13-16}, challenging the current approaches in cryo-
56 EM structure determination^{6-9,17-19}. Visualizing atomic structures of transient, nonequilibrium
57 intermediates connecting the major states of the proteasome has been unsuccessful by
58 conventional cryo-EM analysis^{1,2,9,16,18,19}. To address this major challenge, we developed a novel
59 deep manifold learning system codenamed AlphaCryo4D that can break such a limitation and
60 enable atomic-level cryo-EM reconstructions of highly dynamic, lowly populated intermediates
61 or transient states. By applying AlphaCryo4D to analyze a large cryo-EM dataset that previously
62 solved the atomic structures of 7 proteasomal RP-CP states², we reconstructed 64 conformers of
63 the human 26S proteasome in the act of substrate degradation up to 2.5-Å resolution. Systematic
64 analyses of those transient or intermediate states in substrate processing pinpoint energetic
65 differences between the doubly and singly capped proteasomes, discover several novel ubiquitin-
66 binding sites in the proteasome, and choreograph single-nucleotide-exchange dynamics of the
67 proteasomal AAA-ATPase motor during translocation initiation. Importantly, the dramatically

68 enriched proteasomal states provide unprecedented insights into an integrative, hierarchical
69 allosteric mechanism of proteasome autoregulation upon polyubiquitylated substrate interactions.
70

71 **Design of deep manifold learning**

72 The conceptual framework of AlphaCryo4D integrates unsupervised 3D deep learning with
73 manifold embedding to learn a free-energy landscape, which directs single-particle cryo-EM
74 reconstructions of rare transient states via an energy-based particle-voting algorithm. In brevity,
75 AlphaCryo4D involves four major steps of data processing (Fig. 1a, Extended Data Fig. 1; see
76 Methods for details): (1) Hundreds to thousands of 3D volumes are bootstrapped with M -fold
77 data augmentation by particle shuffling and Bayesian clustering¹⁹, during which each particle is
78 used M times in reconstructing M volumes; each of the M copies is called a ‘vote’ of the particle
79 (Extended Data Fig. 1a). (2) 3D feature maps of all volumes are learnt by an autoencoder²⁰ made
80 of a 3D deep residual neural network³ and are used to compute a free-energy landscape through
81 manifold embedding^{4,5} (Fig. 1b, d, e, Extended Data Table 1). (3) A string method²¹ is used to
82 search the minimum energy path (MEP) on the free-energy landscape²², which defines the local
83 energy minima or transition states of interest as the centers of the clustering boundaries for
84 particle voting (Fig. 1f). (4) Each particle is counted for the number of votes that are casted
85 within the voting boundaries on the energy landscape. The particle is classified to the cluster that
86 receives more than $M/2$ votes of this particle within its voting boundary (Fig. 1f, Extended Data
87 Fig. 1b). Particles that cannot be reproducibly voted into any clustering boundaries for more than
88 $M/2$ times are ‘voted out’ during this procedure. The resulting 3D classes are expected to be
89 conformationally homogeneous enough for high-resolution cryo-EM refinement⁸. Since many
90 protein complexes exhibit profound conformational changes in different local regions, we also
91 implemented a focused classification strategy of AlphaCryo4D that applies a local 3D mask¹⁸
92 throughout the entire procedure, often being executed as an iterative step after initial 3D
93 classification by AlphaCryo4D in the absence of any 3D mask (Fig. 1a, Methods).

94

95 **Solving conformational continuum at atomic level**

96 To assess the numerical performance of AlphaCryo4D, we generated three large synthetic
97 heterogeneous cryo-EM datasets with signal-to-noise ratios (SNRs) of 0.05, 0.01 and 0.005.
98 Each dataset includes 2 million randomly oriented single particles computationally simulated

99 from 20 hypothetical conformer models of the ~130-kDa NLRP3 inflammasome protein²³. These
100 conformers imitate continuous conformational changes of the NACHT domain rotating around
101 the LRR domain over an angular range of 90° during inflammasome activation²³ (Fig. 1c). We
102 conducted blind assessments on 3D classification and heterogeneous reconstructions by
103 AlphaCryo4D, without providing any information of particle orientation and conformational
104 identities (Fig. 1d-f, Extended Data Fig. 2). The 3D classification precision of a retrieved
105 conformer was computed as the ratio of the particle number of correct class assignment (based
106 on the ground truth) versus the total particle number in the class. The results of AlphaCryo4D
107 were then compared with several conventional methods, including maximum-likelihood-based
108 3D (ML3D) classification in RELION^{8,9,18} and 3D principal component analysis (PCA) in
109 cryoSPARC⁷. In all blind tests, AlphaCryo4D retrieved all 20 conformers and markedly
110 outperformed the conventional methods, with an average of 3D classification precision at 0.83,
111 0.82 and 0.65 for datasets with SNRs of 0.05, 0.01 and 0.005, respectively (Fig. 2a, Extended
112 Data Fig. 3a-c). By contrast, the conventional methods missed two to six conformers entirely and
113 exhibited 3D classification precisions in the range of 0.2-0.5 in general (Fig. 2b, c, Extended
114 Data Figs. 3d-l, 4).

115 The 3D classification precision appears to be strongly correlated with the map quality and
116 resolution homogeneity across the density map (Fig. 2). All 20 density maps from AlphaCryo4D
117 consistently show homogeneous resolutions at 2.6-2.9 Å between the NACHT and LRR domains
118 (Fig. 2d, g, Extended Data Figs. 3m, 4a). By contrast, all density maps by the conventional
119 methods show lower average resolutions and notably heterogeneous local resolutions, with the
120 NACHT domain exhibiting substantially lower resolution than that of the LRR domain, causing
121 blurred features, broken loops and invisible sidechains in NACHT (Fig. 2e, f, h, i, Extended Data
122 Figs. 3n, o, 4b, c). Thus, the significantly improved 3D classification accuracy by AlphaCryo4D
123 enables 4D reconstructions of conformational continuum at the atomic level.

124 To understand how the 3D classification accuracy is improved in AlphaCryo4D, we further
125 studied the algorithmic mechanism by tracking the statistical distributions of classification
126 precisions over intermediate steps of data processing (Extended Data Fig. 5). We found that the
127 steps of particle shuffling, defining cluster boundaries on the manifold-embedded free-energy
128 landscapes and energy-based particle-voting contribute to ~16%, ~20% and ~40% improvements
129 in the distributions of high-precision 3D classes, respectively, suggesting that our design of the

130 particle-voting algorithm considerably improves the performance of AlphaCryo4D, without
131 which deep learning alone is insufficient to achieve the present level of 3D classification
132 accuracy.

133

134 **Visualizing hidden dynamics of the proteasome**

135 Having conducted the proof-of-principle study of AlphaCryo4D using simulated datasets, we
136 then turned to several experimental datasets^{2,15}. We first applied this approach to analyze an
137 existing cryo-EM dataset of the substrate-free ATP γ S-bound 26S proteasome¹⁵. The
138 AlphaCryo4D-reconstructed energy landscape clearly shows six local energy minima
139 corresponding to the known six conformational states S_A, S_B, S_C, S_{D1}, S_{D2} and S_{D3}, verifying the
140 applicability of AlphaCryo4D in processing real experimental data¹⁵ (Fig. 3a). Next, we used
141 AlphaCryo4D and its focused classification procedure to analyze a larger cryo-EM dataset of the
142 substrate-engaged 26S proteasome (Fig. 3b, c, Extended Data Fig. 6 and Methods)². This dataset
143 was collected on the human 26S proteasome mixed with a Lys63-linked polyubiquitinated
144 substrate Sic1^{PY} for 30 seconds before ATP was diluted with ATP γ S, which was expected to
145 maximally capture any intermediate states before the degradation reaction was completed². The
146 reconstruction of the free energy landscape of the substrate-engaged proteasome suggests that the
147 rate-limiting step of substrate degradation lies in the initiation of substrate unfolding after
148 substrate deubiquitylation, reflected in the highest activation energy barrier between states E_B
149 and E_{C1} (Fig. 3b, c), consistent with a recent fluorescence microscopy study on the proteasome
150 kinetics²⁴.

151 Impressively, AlphaCryo4D extracted significantly more conformers of the proteasomes in
152 various forms from the same cryo-EM dataset that previously yielded seven atomic structures of
153 the proteasome². It discovered 20 conformational states of RP-CP subcomplex (Fig. 3b, c,
154 Extended Data Fig. 7, Extended Data Table 2). Eight transient states (designated E_{A1.2}, E_{A2.2},
155 E_{A2.3}, E_{B.2}, E_{B.3}, E_{D2.2}, E_{D2.3} and E_{D.α5}) at 3.1-7.5 Å resolution exhibit previously unseen features
156 of ubiquitin that map various ubiquitin-binding sites on the RPN1, RPN2, RPN10 and α5
157 subunits in the proteasome (Fig. 4). Six sequential intermediate states (designated E_{D0.1}, E_{D0.2},
158 E_{D0.3}, E_{D1.1}, E_{D1.2} and E_{D1.3}) at 3.2-3.9 Å resolution bridge a major missing gap between states
159 E_{C2} and E_{D1}, revealing how concerted structural transitions in the AAA-ATPase motor during

160 single-nucleotide exchange drive the initiation of substrate unfolding (Fig. 5, Extended Data Fig.
161 7c, g-i).

162 To understand whether the singly capped (SC) and doubly capped (DC) proteasomes behave
163 differently, AlphaCryo4D reconstructed 8 and 36 conformational states for the pure SC and DC
164 holoenzymes, respectively (Fig. 3d, e, Extended Data Figs. 8, 9). All 8 SC and 29 DC states were
165 refined to 3.7-4.7 Å, with 7 DC states limited to 6-9 Å due to their transient nature and extremely
166 low population (Extended Data Fig. 8b, e, f). Note that the CP gate in the RP-distal side of the 20
167 states of RP-CP subcomplex is in a heterogeneous conformation of various stoichiometric ratios
168 between closed and open states. By contrast, both CP gates in the 44 states of pure SC or DC
169 reconstructions are in a homogeneous conformation.

170 Besides resolving significantly more conformers, AlphaCryo4D pushes the envelope of the
171 achievable resolution of known states due to its advantage in keeping more particles without
172 sacrificing conformational homogeneity. For example, the structure of state E_{D2} was improved
173 from previous resolution at 3.2 Å to 2.5 Å, allowing us to investigate how the CP gating
174 allosterically regulates the catalytic activity of the β-type subunits (Fig. 6, Extended Data Fig. 7c,
175 g-i). The local resolution of RPN11-bound ubiquitin in state E_{A2} was also improved from 5-6 Å
176 to 3.5 Å among many other improvements (Extended Data Fig. 10a).

177

178 **Conformational entanglement**

179 Both the SC and DC proteasomes are abundant in cells²⁵. Their structural and functional
180 difference, however, remains elusive. In the 36 DC reconstructions, each conformer is a
181 combination of two RP states. Each CP gate in the DC proteasome appears to be rigorously
182 controlled by their respective proximal RP and is only open when its proximal RP is in an E_D-
183 compatible state with five RPT C-terminal tails inserted into the surface pockets on the α-ring²
184 (Fig. 3e, Extended Data Fig. 8a-d). Consistently, the gate on the RP-free side of the CP in the SC
185 proteasome is closed in all states, indicating the CP gate opening on the RP-controlled side does
186 not remotely open the other CP gate on the RP-free side (Extended Data Fig. 8d).

187 To understand whether the conformational states of two RPs in the DC proteasome
188 allosterically influence each other, we compare the state distribution matrix obtained by
189 AlphaCryo4D to the prediction of a control model assuming two completely uncoupled RP states
190 in the DC proteasome (Fig. 3f-h). Although the overall pattern of the experimental distribution

191 roughly agrees with the model prediction, a notable number of DC states exhibit substantial
192 deviation, indicating that the conformational dynamics of the two RPs in the same proteasome
193 are profoundly entangled together (Fig. 3g, h). Intriguingly, the most prominent positive
194 deviations are seen in the state distributions of E_B-E_B, E_B-E_{D2}, and E_{D2}-E_{D2} combinations (Fig.
195 3g), suggesting that the deubiquitylation state E_B and the translocation state E_{D2} of one RP are
196 allosterically coupled to and mutually upregulated by states E_B and E_{D2} of the opposite RP.
197 Coupled actions of deubiquitylation and translocation between two opposite RPs are expected to
198 optimize the efficiency of substrate processing. Moreover, all the DC states along the diagonal of
199 the state distribution matrix are more or less upregulated (indicated by red in Fig. 3g, h),
200 suggesting that both RPs in the same proteasome synergistically promote each other to transit
201 into downstream states in a symmetrical fashion.

202 Notably, the largest discrepancy of the distribution of RP states between the SC and DC
203 proteasomes also lies in state E_B (Fig. 3b-d). The state population of E_B is significantly lower in
204 the SC than in the DC proteasome. This observation verifies the conclusion drawn from the
205 above analysis on the DC proteasomes alone that state E_B is upregulated by the conformational
206 entanglement effect in the DC holoenzyme, suggesting that the SC proteasome lacks the
207 functional synergy between two opposite RPs seen in the DC proteasome (Fig. 3h). Altogether,
208 these results implicate that the DC proteasome could be energetically more efficient in substrate
209 deubiquitylation and degradation than the SC proteasome.

210

211 **Novel ubiquitin-binding sites**

212 Unexpectedly, in states E_{A1.2}, E_{A2.2}, and E_{B.2}, a diubiquitin-like density is consistently found on
213 RPN2, whereas a monoubiquitin-like density is observed at the apex of the von Willebrand
214 factor type A (VWA) domain of RPN10 in states E_{A2.3}, E_{B.3} and E_{D2.3} (Fig. 4a, Extended Data
215 Fig. 10b-f). In state E_{D2.2}, the diubiquitin-like density, however, appears to contact both RPN2
216 and RPN10, and can be modelled with a Lys63-linked diubiquitin (Extended Data Fig. 10b, f).
217 The RPN10 ubiquitin-interacting motifs (UIMs), however, were not reliably observed
218 presumably due to their highly flexible nature (Extended Data Fig. 10f). The populations of these
219 states are very small and represented in only a few thousand particles or 0.1-0.3% of the entire
220 dataset, indicating their transient nature. The local resolutions of the RPN2- and RPN10-bound
221 ubiquitin-like densities are lower than the rest of the reconstructions and other ubiquitin densities

222 on RPN1, RPN11 and α 5 subunits. Rigid-body fitting of the ubiquitin structure into these
223 ubiquitin-like densities confirms the agreement of the overall density shape with the ubiquitin
224 structure (Fig. 4a, Extended Data Fig. 10b, c, f).

225 The ubiquitin-binding site on RPN2 is centered on three helices harboring an acidic surface
226 around residues Tyr502, Glu530, Asp531 and Ser569 (Fig. 4b-e). Structural comparison suggests
227 that the ubiquitin-binding site on RPN2 is homologous to the T1 site of RPN1 (Fig. 4c, d)¹². We
228 therefore name it ‘the RPN2 T1 site’. Although there is little conservation in amino acid
229 sequences between the RPN1 and RPN2 T1 sites, their structural and electrostatic properties are
230 highly conserved (Fig. 4d, Extended Data Fig. 10g-j). Comparison with the NMR structure of
231 Lys48-linked diubiquitin-bound RPN1 T1 site helices¹² further confirms the conservation and
232 similarity of the ubiquitin-binding modes between the RPN1 and RPN2 T1 sites (Fig. 4c).
233 Consistent with this finding, previous studies have observed weak interactions of ubiquitin-like
234 (UBL) protein with RPN2 by cross-linking experiments²⁶. As there is also ubiquitin bound to
235 RPN11 in states E_{A2.2}, and E_{B.2}, a Lys63-linked triubiquitin chain can be fitted into the RPN2-
236 and RPN11-bound ubiquitin densities by modeling the rotation of Lys63 linkages, suggesting
237 that the RPN2 T1 site may function as a coreceptor site for ubiquitin transfer from RPN10 to
238 RPN11 to facilitate deubiquitylation (Fig. 4g). Given that at least one RPN10 UIM-bound
239 ubiquitin invisible in these cryo-EM maps would be expected to exist, the observation of
240 triubiquitin on RPN2 and RPN11 structurally rationalizes why tetraubiquitin is an optimal
241 degradation signal for the proteasome¹.

242 By focused 3D classification via AlphaCryo4D, we refined the RPN1 with ubiquitin binding
243 its T2 site¹² in state E_{A1} to 3.7 Å, which was previously reconstructed at moderate resolution (~5
244 Å) (Extended Data Fig. 10d). This allows us to visualize the RPN1 T2 site in atomic detail,
245 revealing that the ubiquitin-contacting surface is composed of residues Asp423, Leu426,
246 Asp430, Glu458, Cys459, and Asp460 from two helices (Fig. 4c, d), representing a footprint that
247 is slightly larger than the yeast Rpn1 T2 site for Ubp6 interaction¹². Previous data have suggested
248 that RPN1 T2 site is a receptor site for UBL proteins like Ubp6 and USP14 with lack of evidence
249 for ubiquitin binding¹². Our direct observation of ubiquitin binding at this site revises such a
250 conception, suggesting that the RPN1 T2 may be also a primary ubiquitin receptor site.

251 In state E_{D2.2}, we can observe a ubiquitin density bound to the RPN1 T2 site and another
252 weaker ubiquitin density at the α 5-subunit ~6 nm beneath the RPN1 T2 site (Fig. 4a, Extended

253 Data Fig. 10b). To understand if the ubiquitin-binding site on the $\alpha 5$ subunit is used more
254 broadly, we combined all the E_D-compatible states and focused the 3D classification of
255 AlphaCryo4D on the $\alpha 5$ -bound ubiquitin. This yielded a much larger 3D class, named state E_{D, $\alpha 5$}
256 (~4% of the entire dataset) that improved the ubiquitin-bound CP structure to 3.1 Å, and the $\alpha 5$ -
257 bound ubiquitin density to 4-4.5 Å (Extended Data Figs. 7e.). The ubiquitin-binding site in the
258 $\alpha 5$ subunit is composed of acidic or hydrophobic residues Glu183, Val184, His186, Ser188 and
259 Glu193 in a loop connecting two helices, highly resembling the mode of ubiquitin binding to an
260 RPN13 loop^{11,27} (Fig. 4f, Extended Data Fig. 10e). The electrostatic property of this site is also
261 similar to those of the RPN1 T1, T2 and RPN2 T1 sites that are all acidic, in charge
262 complementarity with the basic ubiquitin surface around residues Ile44 and His68 (Extended
263 Data Fig. 10g-n).

264 We note that these new ubiquitin-binding sites all reside in the vicinity of primary receptor
265 sites. The RPN2 T1 site is very close to the RPN10 UIMs, whereas the $\alpha 5$ site is near the RPN1
266 T2 site. Modelling of a Lys63-linked tetraubiquitin chain by fitting its terminal ubiquitin into the
267 cryo-EM density suggests that a single tetraubiquitin can span across the $\alpha 5$ subunit and the
268 RPN1 T2 site (Fig. 4h). Given that RPN1 appears to allosterically regulate the AAA-ATPase
269 motor conformation² (Fig. 5a, b), tetraubiquitin binding to both the RPN1 T2 site and $\alpha 5$ subunit
270 could allosterically stabilize the open-CP states (E_{D0}, E_{D1} and E_{D2}). It is unclear whether these
271 low-affinity ubiquitin-binding sites would directly involve in primary targeting of substrate-
272 conjugated polyubiquitin chains by the proteasome in cells. However, it is conceivable that the
273 polyubiquitin chains could be first captured by the high-affinity sites and then moved to the
274 nearby low-affinity sites. Working together, these ubiquitin-binding sites could remodel
275 polyubiquitin chains and deliver the peptide-proximal ubiquitin to the deubiquitylation site² (Fig.
276 4g) as well as assist ubiquitin recycle after isopeptide bond hydrolysis (Fig. 4h). We expect that
277 our structural definition of these novel ubiquitin-binding sites would stimulate future functional
278 tests required to understand their biological importance in cells.

279

280 **Single-nucleotide exchange dynamics**

281 The six intermediate states (E_{D0.1}, E_{D0.2}, E_{D0.3}, E_{D1.1}, E_{D1.2} and E_{D1.3}) during initiation of substrate
282 unfolding and translocation exhibit highly coordinated movements in the RP relative to the CP
283 (Fig. 5a-c, Extended Data Fig. 11), with prominent rotations in the RPN1 N-terminal that

284 detaches from RPT6 in states E_{D0.1}, E_{D0.2}, and E_{D0.3} and re-binds RPT6 in state E_{D1.1}, E_{D1.2} and
285 E_{D1.3}. All six conformations share the same architecture in their substrate interactions with pore-1
286 loops from four RPT subunits (RPT2, RPT6, RPT3 and RPT4), which remain largely unchanged
287 in overall conformation (Fig. 5d). These structures illustrate that the RPT2 re-association with
288 the substrate proceeds that of RPT1 after both RPT1 and RPT2 are dissociated from the substrate
289 in state E_C. They also share the same pattern of nucleotide states, with ATP bound to RPT1,
290 RPT2, RPT6 and RPT3 and ADP bound to RPT4. There are poor, partial nucleotide densities in
291 the RPT5 nucleotide-binding pocket, which give rise to the highest B-factor (250-500) when
292 fitted with ADP, suggesting that RPT5 undergoes ADP release in these states (Extended Data
293 Fig. 11k).

294 Markedly, the pore-1 loop of RPT1 gradually moves toward the substrate from a distance of
295 ~16 Å to ~3 Å, whereas the pore-1 loop of RPT5 gradually moves away from the substrate from
296 a distance of ~3 Å to ~16 Å (Fig. 5d, f). The small AAA subdomain of RPT5 moves inward
297 together with the large AAA subdomain of RPT1, as the large AAA subdomain of RPT5 rotates
298 away from the substrate (Extended Data Fig. 11f-i). Consistently, the arginine fingers (R-finger)
299 of RPT2 are progressively moved toward ATP bound in RPT1, closing up the nucleotide-binding
300 pocket (Fig. 5e, g). In contrast, the nucleotide-binding pocket of RPT5 is gradually shrunk but is
301 not fully closed by the R-fingers of RPT1, whereas the nucleotide-binding pocket of RPT4 is
302 gradually opened up (Fig. 5g). As a result, the pore-1 loops of RPT1 and RPT5 are only in
303 contact with the substrate in the last and first states E_{D1.3} and E_{D0.1}, respectively. Both are
304 dissociated from the substrate in states E_{D0.2}, E_{D0.3}, E_{D1.1}, and E_{D1.2}. These gradual movements
305 allow us to assign their temporal sequences as illustrated (Fig. 5a-e), indicating that these states
306 represent intermediate conformations accompanying single-nucleotide exchange that occurs in
307 the RPT5 (Fig. 5h). Interestingly, the outward flipping of RPT5 appears to complete its major
308 conformational change in state E_{D0.3}, much faster than the inward motion of RPT1, which
309 completes its conformational change in state E_{D1.3}. This observation suggests that ATPase re-
310 engagement with the substrate is the rate-limiting step in the single-nucleotide exchange kinetics
311 of the AAA-ATPase motor.

312 Our data clarify that the CP gate is open once the pore-1 loop of RPT2 binds the substrate in
313 state E_{D0.1}, as five RPT C-tails are inserted in the α-pockets in all six states (Extended Data Fig.
314 8c). Altogether, these structures vividly characterize at the atomic level how the “hand-over-

315 hand” actions of RPT subunits are executed by coordinated conformational dynamics in the
316 AAA-ATPase motor during single-nucleotide exchange and generates mechanical force
317 unfolding the substrate. Although the sequential model of coordinated ATP hydrolysis around
318 the AAA-ATPase ring has been hypothesized in numerous similar systems^{1,2,13,16,28}, our results
319 provide the first direct evidence for sequential intermediate states of hand-over-hand actions
320 within a single cycle of nucleotide exchange.

321

322 **Hierarchical allosteric regulation of proteolytic activity**

323 Both atomic structures of the substrate-bound CPs in the open- and closed-gate states E_A and E_{D2}
324 show a segment of substrate polypeptide binding the catalytically active residue Thr1 in the β2
325 subunit, whereas no substrate density is observed in the other two catalytic subunits β1 and β5.
326 In both states, the substrate is bound in a β-sheet conformation between residues 20 to 22 and 46
327 to 48 in the β2 subunit (Fig. 6a, b, Extended Data Fig. 12), reminiscent of the conformations of
328 CP inhibitors binding the β5 subunits in the crystal structures of the CP^{29,30}. The hydroxyl
329 oxygen atom in the catalytic Thr1 is ~2-Å closer to the substrate mainchain in state E_{D2}
330 compared to state E_A. This structural difference is expected to result from the CP gate opening
331 that exerts a profound allosteric impact on the entire CP structure.

332 To understand how such a subtle structural change influences the proteolytic activity, we
333 carried out first-principles calculations of the quantum-mechanical interactions involved in the
334 nucleophilic attack of the catalytic residue Thr1 on the scissile peptide bond in the substrate,
335 using the density functional theory (DFT) with the generalized gradient approximation³¹. To
336 initiate the nucleophilic attack, the carbonyl group needs to be brought to the proximity of the
337 electrophile Thr1-O_y to facilitate the quantum-mechanical interactions^{32,33}. We calculated the
338 charge density difference induced around the interacting pair after proton transfer from Thr1-O_y
339 to Thr1-NH₂ and plotted the contour maps (Fig. 6c, d, Extended Data Fig. 12e, f). It is seen that
340 the substrate-interacting pair of atoms in state E_{D2} start to form a bonding region of slight
341 positive charge difference linking the carbonyl group of the substrate and the Thr1-O_y. By
342 contrast, the pair are too far apart to interact and are well separated by a charge depletion non-
343 bonding region in state E_A. Indeed, a recent study has found that the nucleophilic attack is the
344 rate-limiting step in the acylation barrier using the yeast CP structure in the gate-closed state³³.
345 Our result suggests that CP gate opening allosterically promotes the nucleophilic attack by

346 lowering the activation energy barrier of acylation and induces hybridization of the molecular
347 orbitals, hence upregulating the reaction rate of proteolysis. In support of our structural finding,
348 previous studies have observed indirect evidence for coupling of the CP gating with the
349 proteolytic activity^{34,35}.

350 Taken together, our systematic structural analyses point to a grand allostery model for the
351 proteasomal autoregulation of proteolytic activity through a three-tier hierarchy of inter-
352 molecular interaction networks (Fig. 6e), in which all subunit conformations are allosterically
353 coupled. The first tier of autoregulation is between the CP gate in the α -ring and the catalytic
354 sites of the β -subunits. Opening of the CP gate allosterically upregulates the proteolytic activity
355 of the three β -subunits. The second tier of autoregulation lies between the substrate-bound AAA-
356 ATPase motor and the rest of the proteasome. The AAA-ATPase motor bridges the ubiquitin-
357 binding sites and the CP via direct interactions of the RPT coiled-coil (CC) domains with RPN1,
358 RPN2 and RPN10 harboring ubiquitin-binding sites. As a result, three modes of coordinated
359 ATP hydrolysis appear to regulate the intermediate steps of substrate processing^{1,2}, in which
360 initiation of substrate unfolding is allosterically coupled with CP gating during E_{C2} to E_{D0.1}
361 transition (Fig. 5). The third tier of autoregulation is via dynamic interactions between ubiquitin
362 signals and a collection of ubiquitin receptor sites and deubiquitinases. This is manifested as the
363 dual roles of ubiquitin-binding sites in recognizing ubiquitin signals and in transmitting such
364 recognitions to allosteric regulation of AAA-ATPase conformations that control the CP gate.
365 Ubiquitin binding and remodeling destabilizes the resting state of the proteasome and promotes
366 its transition to states E_B, E_C and ultimately E_D. On the other hand, a polyubiquitin chain binding
367 multiple sites in the proteasome could have profound allosteric and conformational selection
368 effects (Fig. 4g, h). Such three-tier, hierarchical allosteric regulations may occur mutually with
369 both RPs and are expected to underlie the conformational entanglement of the two RPs in the DC
370 proteasome (Fig. 3e), which was not clearly observed in the absence of substrates^{15,36}. This grand
371 allostery mechanism might have been evolved to optimize the proteasome function in response
372 to extremely complicated intracellular challenges and is manifested as various phenotypic
373 effects, such as UBL-induced proteasome activation^{37,38}, long-range allosteric regulation of RP
374 by CP inhibitors³⁵ and allosteric coupling of two opposite α -ring gates in the archaeal CP³⁹.
375

376 **Concluding remarks**

377 In this work, motivated by solving the hidden dynamics of proteasome autoregulation, we
378 developed AlphaCryo4D, a novel framework of deep manifold learning, that enables 3D
379 reconstructions of nonequilibrium conformational continuum at the atomic level. In
380 retrospective, finding novel ubiquitin-binding sites in the proteasome, choreographing sequential
381 intermediates within a single cycle of nucleotide exchange, and detecting conformational
382 entanglement of the two RPs in the DC holoenzyme as well as subtle allosteric effects of
383 polypeptide hydrolysis by CP gating, each itself presents a formidable challenge. Being able to
384 accomplish all these missions on a single experimental dataset by solving 64 proteasomal states
385 demonstrates that AlphaCryo4D is a major advancement of deep learning in solving 3D
386 heterogeneity problems in cryo-EM structure analysis and showcases tremendous potentials of
387 deep learning in transforming cryo-EM and molecular imaging. More importantly, AlphaCryo4D
388 revealed ‘previously invisible’ mechanistic details in nonequilibrium transient interactions of the
389 proteasome with polyubiquitylated substrates and offered unprecedented insights into the grand
390 hierarchical allostery underlying the proteasome activity and function. With recent
391 improvements in cryo-EM instruments^{40,41} and time-resolved sample preparation methods^{42,43},
392 we expect that current development and future widespread applications of AlphaCryo4D or
393 similar approaches will considerably boost the capability of cryo-EM imaging as a de novo
394 discovery tool and transform modern research in physical and molecular biology.
395

396 References

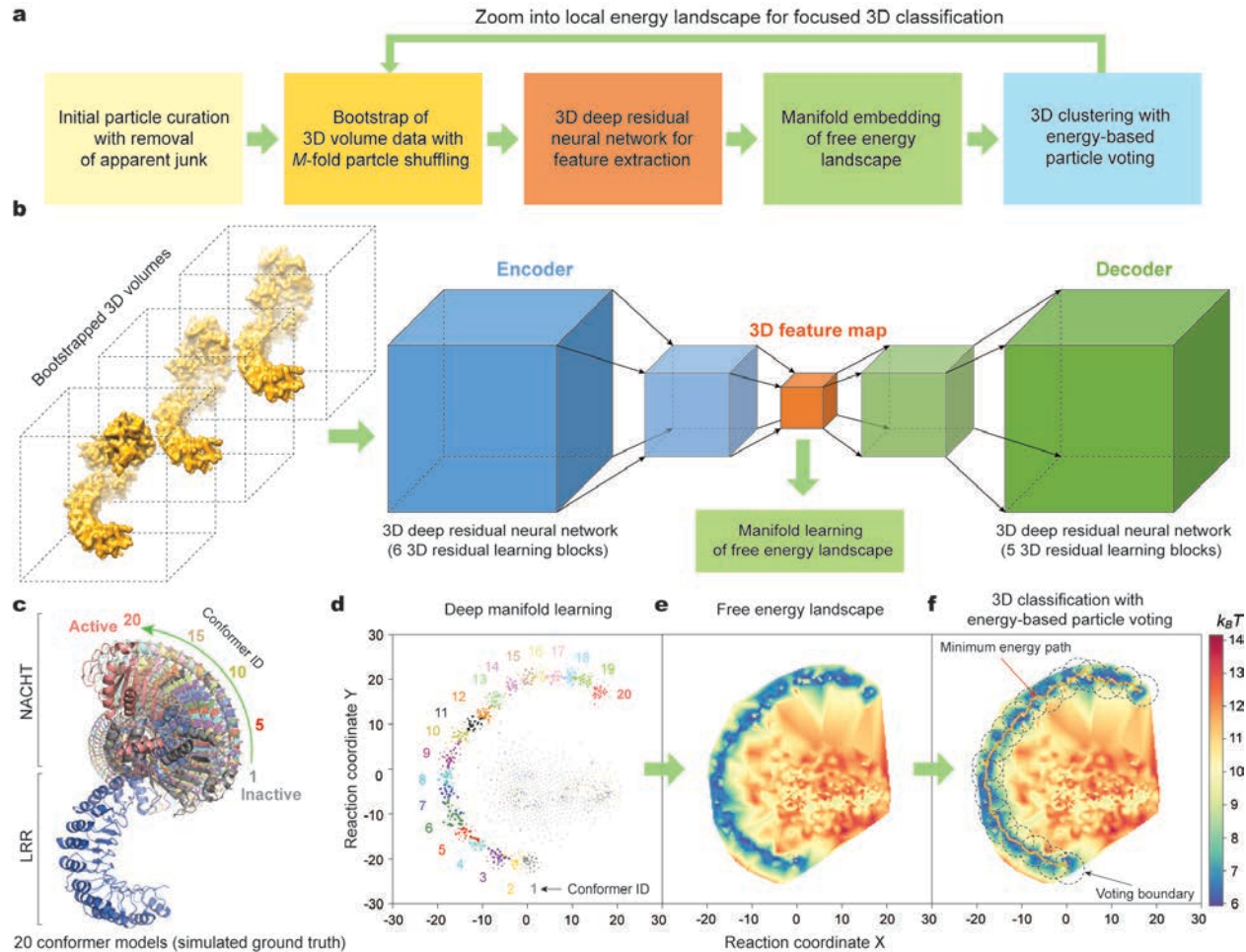
- 397 1 Mao, Y. Structure, Dynamics and Function of the 26S Proteasome. In: Harris J.R.,
398 Marles-Wright J. (eds) Macromolecular Protein Complexes III: Structure and Function.
399 *Subcell Biochem* **96**, 1-151, doi:10.1007/978-3-030-58971-4_1 (2021).
- 400 2 Dong, Y. *et al.* Cryo-EM structures and dynamics of substrate-engaged human 26S
401 proteasome. *Nature* **565**, 49-55, doi:10.1038/s41586-018-0736-4 (2019).
- 402 3 He, K., Zhang, X., Ren, S. & Sun, J. Deep Residual Learning for Image Recognition.
403 *2016 IEEE Conference on Computer Vision and Pattern Recognition (CVPR), Las Vegas,*
404 NV, 770-778, doi:10.1109/CVPR.2016.90 (2016).
- 405 4 van der Maaten, L. & Hinton, G. Visualizing Data using t-SNE. *J Mach Learn Res* **9**,
406 2579-2605 (2008).
- 407 5 Dashti, A. *et al.* Trajectories of the ribosome as a Brownian nanomachine. *Proc Natl
408 Acad Sci U S A* **111**, 17492-17497, doi:10.1073/pnas.1419276111 (2014).
- 409 6 Frank, J. *Three-dimensional electron microscopy of macromolecular assemblies :
410 visualization of biological molecules in their native state*. 2nd edn, (Oxford University
411 Press, 2006).
- 412 7 Punjani, A., Rubinstein, J. L., Fleet, D. J. & Brubaker, M. A. cryoSPARC: algorithms for
413 rapid unsupervised cryo-EM structure determination. *Nat Methods* **14**, 290-296,

- 414
415 8 doi:10.1038/nmeth.4169 (2017).
416 Zivanov, J. *et al.* New tools for automated high-resolution cryo-EM structure
417 determination in RELION-3. *Elife* **7**, doi:10.7554/eLife.42166 (2018).
418 Nakane, T., Kimanis, D., Lindahl, E. & Scheres, S. H. Characterisation of molecular
419 motions in cryo-EM single-particle data by multi-body refinement in RELION. *Elife* **7**,
420 doi:10.7554/eLife.36861 (2018).
421 10 Galves, M., Rathi, R., Prag, G. & Ashkenazi, A. Ubiquitin Signaling and Degradation of
422 Aggregate-Prone Proteins. *Trends Biochem Sci*, doi:10.1016/j.tibs.2019.04.007 (2019).
423 Husnjak, K. *et al.* Proteasome subunit Rpn13 is a novel ubiquitin receptor. *Nature* **453**,
424 481-488, doi:10.1038/nature06926 (2008).
425 12 Shi, Y. *et al.* Rpn1 provides adjacent receptor sites for substrate binding and
deubiquitination by the proteasome. *Science* **351**, doi:10.1126/science.aad9421 (2016).
426 13 Zhang, S. & Mao, Y. AAA+ ATPases in Protein Degradation: Structures, Functions and
427 Mechanisms. *Biomolecules* **10**, doi:10.3390/biom10040629 (2020).
428 14 Chen, S. *et al.* Structural basis for dynamic regulation of the human 26S proteasome.
429 *Proc Natl Acad Sci U S A* **113**, 12991-12996, doi:10.1073/pnas.1614614113 (2016).
430 15 Zhu, Y. *et al.* Structural mechanism for nucleotide-driven remodeling of the AAA-
431 ATPase unfoldase in the activated human 26S proteasome. *Nat Commun* **9**, 1360,
432 doi:10.1038/s41467-018-03785-w (2018).
433 16 de la Pena, A. H., Goodall, E. A., Gates, S. N., Lander, G. C. & Martin, A. Substrate-
434 engaged 26S proteasome structures reveal mechanisms for ATP-hydrolysis-driven
435 translocation. *Science* **362**, doi:10.1126/science.aav0725 (2018).
436 17 Wu, J. *et al.* Massively parallel unsupervised single-particle cryo-EM data clustering via
437 statistical manifold learning. *PLoS One* **12**, e0182130, doi:10.1371/journal.pone.0182130
(2017).
438 18 Scheres, S. H. Processing of Structurally Heterogeneous Cryo-EM Data in RELION.
439 *Methods Enzymol* **579**, 125-157, doi:10.1016/bs.mie.2016.04.012 (2016).
440 19 Scheres, S. H. *et al.* Disentangling conformational states of macromolecules in 3D-EM
441 through likelihood optimization. *Nat Methods* **4**, 27-29, doi:10.1038/nmeth992 (2007).
442 20 Hinton, G. E. & Salakhutdinov, R. R. Reducing the dimensionality of data with neural
443 networks. *Science* **313**, 504-507, doi:10.1126/science.1127647 (2006).
444 21 E, W., Ren, W. & Vanden-Eijnden, E. String method for the study of rare events. *Phys
445 Rev B* **66**, 052301 (2002).
446 22 E, W., Ren, W. & Vanden-Eijnden, E. Simplified and improved string method for
447 computing the minimum energy paths in barrier-crossing events. *J Chem Phys* **126**,
448 164103, doi:10.1063/1.2720838 (2007).
449 23 Sharif, H. *et al.* Structural mechanism for NEK7-licensed activation of NLRP3
450 inflammasome. *Nature* **570**, 338-343, doi:10.1038/s41586-019-1295-z (2019).
451 24 Bard, J. A. M., Bashore, C., Dong, K. C. & Martin, A. The 26S Proteasome Utilizes a
452 Kinetic Gateway to Prioritize Substrate Degradation. *Cell* **177**, 286-298 e215,
453 doi:10.1016/j.cell.2019.02.031 (2019).
454 25 Asano, S. *et al.* Proteasomes. A molecular census of 26S proteasomes in intact neurons.
455 *Science* **347**, 439-442, doi:10.1126/science.1261197 (2015).
456 26 Saeki, Y., Sone, T., Toh-e, A. & Yokosawa, H. Identification of ubiquitin-like protein-
457 binding subunits of the 26S proteasome. *Biochem Biophys Res Commun* **296**, 813-819,
458 doi:10.1016/s0006-291x(02)02002-8 (2002).
459

- 460 27 Schreiner, P. *et al.* Ubiquitin docking at the proteasome through a novel pleckstrin-
461 homology domain interaction. *Nature* **453**, 548-552, doi:10.1038/nature06924 (2008).
- 462 28 Puchades, C., Sandate, C. R. & Lander, G. C. The molecular principles governing the
463 activity and functional diversity of AAA+ proteins. *Nat Rev Mol Cell Biol* **21**, 43-58,
464 doi:10.1038/s41580-019-0183-6 (2020).
- 465 29 Lowe, J. *et al.* Crystal structure of the 20S proteasome from the archaeon *T. acidophilum*
466 at 3.4 Å resolution. *Science* **268**, 533-539, doi:10.1126/science.7725097 (1995).
- 467 30 Schrader, J. *et al.* The inhibition mechanism of human 20S proteasomes enables next-
468 generation inhibitor design. *Science* **353**, 594-598, doi:10.1126/science.aaf8993 (2016).
- 469 31 Perdew, J. P., Burke, K. & Ernzerhof, M. Generalized Gradient Approximation Made
470 Simple. *Phys Rev Lett* **77**, 3865-3868, doi:10.1103/PhysRevLett.77.3865 (1996).
- 471 32 Groll, M. *et al.* Structure of 20S proteasome from yeast at 2.4 Å resolution. *Nature* **386**,
472 463-471, doi:10.1038/386463a0 (1997).
- 473 33 Saha, A., Oanca, G., Mondal, D. & Warshel, A. Exploring the Proteolysis Mechanism of
474 the Proteasomes. *J Phys Chem B* **124**, 5626-5635, doi:10.1021/acs.jpcb.0c04435 (2020).
- 475 34 Osmulski, P. A., Hochstrasser, M. & Gaczynska, M. A tetrahedral transition state at the
476 active sites of the 20S proteasome is coupled to opening of the alpha-ring channel.
477 *Structure* **17**, 1137-1147, doi:10.1016/j.str.2009.06.011 (2009).
- 478 35 Haselbach, D. *et al.* Long-range allosteric regulation of the human 26S proteasome by
479 20S proteasome-targeting cancer drugs. *Nat Commun* **8**, 15578,
480 doi:10.1038/ncomms15578 (2017).
- 481 36 Eisele, M. R. *et al.* Expanded Coverage of the 26S Proteasome Conformational
482 Landscape Reveals Mechanisms of Peptidase Gating. *Cell Rep* **24**, 1301-1315 e1305,
483 doi:10.1016/j.celrep.2018.07.004 (2018).
- 484 37 Collins, G. A. & Goldberg, A. L. Proteins containing ubiquitin-like (Ubl) domains not
485 only bind to 26S proteasomes but also induce their activation. *Proc Natl Acad Sci U S A*
486 **117**, 4664-4674, doi:10.1073/pnas.1915534117 (2020).
- 487 38 Kim, H. T. & Goldberg, A. L. UBL domain of Usp14 and other proteins stimulates
488 proteasome activities and protein degradation in cells. *Proc Natl Acad Sci U S A* **115**,
489 E11642-E11650, doi:10.1073/pnas.1808731115 (2018).
- 490 39 Yu, Z. *et al.* Allosteric coupling between alpha-rings of the 20S proteasome. *Nat
491 Commun* **11**, 4580, doi:10.1038/s41467-020-18415-7 (2020).
- 492 40 Nakane, T. *et al.* Single-particle cryo-EM at atomic resolution. *Nature* **587**, 152-156,
493 doi:10.1038/s41586-020-2829-0 (2020).
- 494 41 Yip, K. M., Fischer, N., Paknia, E., Chari, A. & Stark, H. Atomic-resolution protein
495 structure determination by cryo-EM. *Nature* **587**, 157-161, doi:10.1038/s41586-020-
496 2833-4 (2020).
- 497 42 Dandey, V. P. *et al.* Time-resolved cryo-EM using Spotiton. *Nat Methods* **17**, 897-900,
498 doi:10.1038/s41592-020-0925-6 (2020).
- 499 43 Kaledhonkar, S. *et al.* Late steps in bacterial translation initiation visualized using time-
500 resolved cryo-EM. *Nature* **570**, 400-404, doi:10.1038/s41586-019-1249-5 (2019).
- 501 44 Zhu, Y., Ouyang, Q. & Mao, Y. A deep convolutional neural network approach to single-
502 particle recognition in cryo-electron microscopy. *BMC Bioinformatics* **18**, 348,
503 doi:10.1186/s12859-017-1757-y (2017).
- 504 45 Bepler, T. *et al.* Positive-unlabeled convolutional neural networks for particle picking in
505 cryo-electron micrographs. *Res Comput Mol Biol* **10812**, 245-247 (2018).

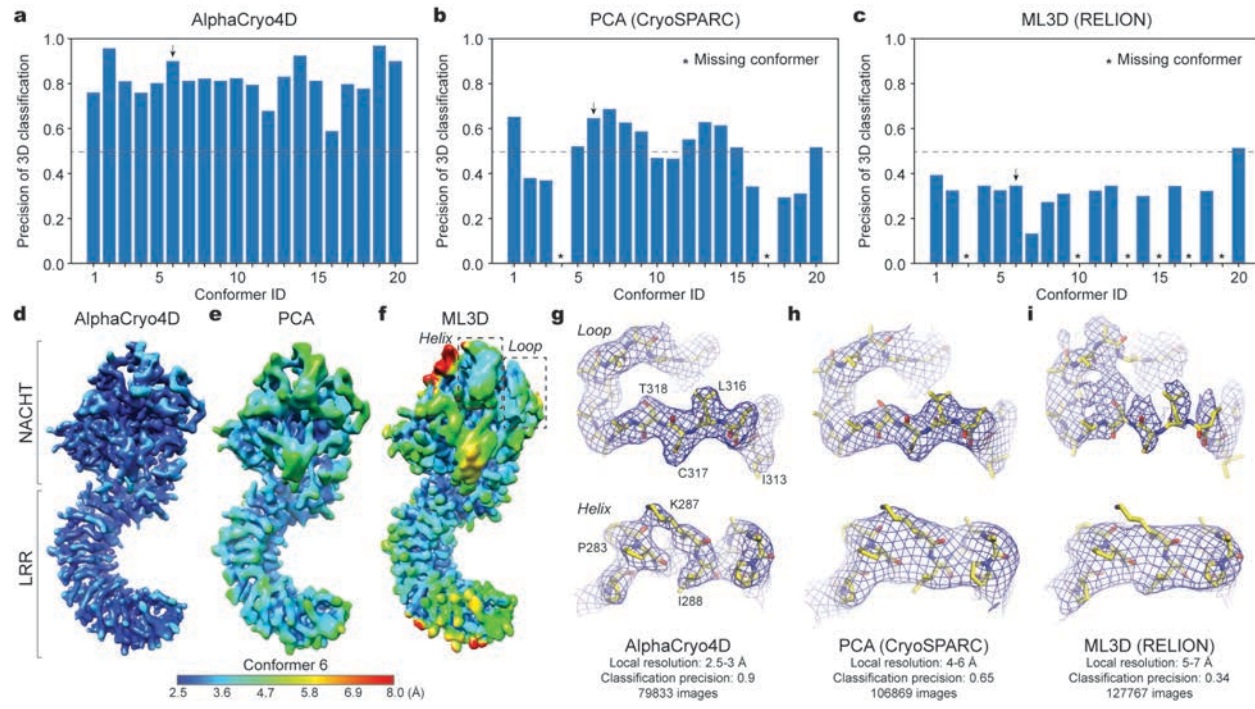
- 506 46 Qian, N. On the momentum term in gradient descent learning algorithms. *Neural Netw*
507 12, 145-151, doi:10.1016/s0893-6080(98)00116-6 (1999).
- 508 47 Unverdorben, P. *et al.* Deep classification of a large cryo-EM dataset defines the
509 conformational landscape of the 26S proteasome. *Proc Natl Acad Sci U S A* **111**, 5544-
510 5549, doi:10.1073/pnas.1403409111 (2014).
- 511 48 Wehmer, M. *et al.* Structural insights into the functional cycle of the ATPase module of
512 the 26S proteasome. *Proc Natl Acad Sci U S A* **114**, 1305-1310,
513 doi:10.1073/pnas.1621129114 (2017).
- 514 49 Emsley, P. & Cowtan, K. Coot: model-building tools for molecular graphics. *Acta
515 Crystallogr D Biol Crystallogr* **60**, 2126-2132, doi:10.1107/S0907444904019158 (2004).
- 516 50 Pettersen, E. F. *et al.* UCSF Chimera--a visualization system for exploratory research and
517 analysis. *J Comput Chem* **25**, 1605-1612, doi:10.1002/jcc.20084 (2004).
- 518 51 Adams, P. D. *et al.* PHENIX: a comprehensive Python-based system for macromolecular
519 structure solution. *Acta Crystallogr D Biol Crystallogr* **66**, 213-221,
520 doi:10.1107/S0907444909052925 (2010).
- 521 52 The PyMOL Molecular Graphics System Version 2.0 (Schrödinger, LLC).
- 522 53 Goddard, T. D. *et al.* UCSF ChimeraX: Meeting modern challenges in visualization and
523 analysis. *Protein Sci* **27**, 14-25, doi:10.1002/pro.3235 (2018).
- 524 54 Kucukelbir, A., Sigworth, F. J. & Tagare, H. D. Quantifying the local resolution of cryo-
525 EM density maps. *Nat Methods* **11**, 63-65, doi:10.1038/nmeth.2727 (2014).
- 526 55 Heymann, J. B. & Belnap, D. M. Bsoft: image processing and molecular modeling for
527 electron microscopy. *J Struct Biol* **157**, 3-18, doi:10.1016/j.jsb.2006.06.006 (2007).
- 528 56 Dolinsky, T. J., Nielsen, J. E., McCammon, J. A. & Baker, N. A. PDB2PQR: an
529 automated pipeline for the setup of Poisson-Boltzmann electrostatics calculations.
530 *Nucleic Acids Res* **32**, W665-667, doi:10.1093/nar/gkh381 (2004).
- 531 57 Soler, J. M. *et al.* The SIESTA method for ab initio order-N materials simulation. *J Phys
532 Condens Matter* **14**, 2745-2779 (2002).

533
534
535
536
537

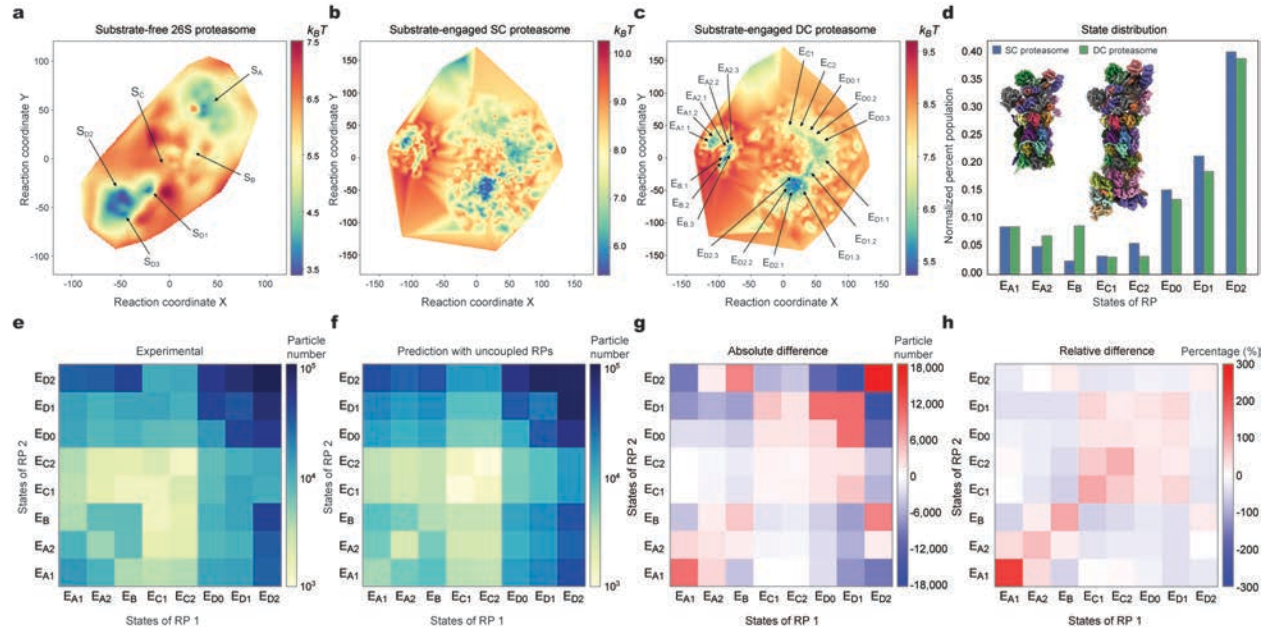


538

539 **Figure 1. Conceptual framework of AlphaCryo4D for 4D cryo-EM reconstruction. a,**
540 Schematic showing the major conceptual steps of single-particle cryo-EM data processing in
541 AlphaCryo4D. **b**, Illustration of deep residual learning of 3D feature maps by an autoencoder
542 conjugated to a decoder for unsupervised training. **c**, The 20 atomic models of hypothetical
543 conformers of NLRP3 in cartoon representations simulate a 90° rotation of the NACHT domain
544 relative to the LRR domain based on the structure of NLRP3 (PDB ID: 6NPY). **d**, Manifold
545 learning of the bootstrapped 3D volumes and their feature maps learnt by the autoencoder. Each
546 data point corresponds to a 3D volume. The color labels the conformer identity of ground truth
547 for the purpose of verification. **e**, Free energy landscape computed from the manifold shown in **d**
548 using the Boltzmann distribution. **f**, Minimum energy path (orange line) calculated by the string
549 method is used to find the approximate cluster centers of 20 conformers. The cluster boundaries
550 for energy-based particle voting are shown as dashed circles.

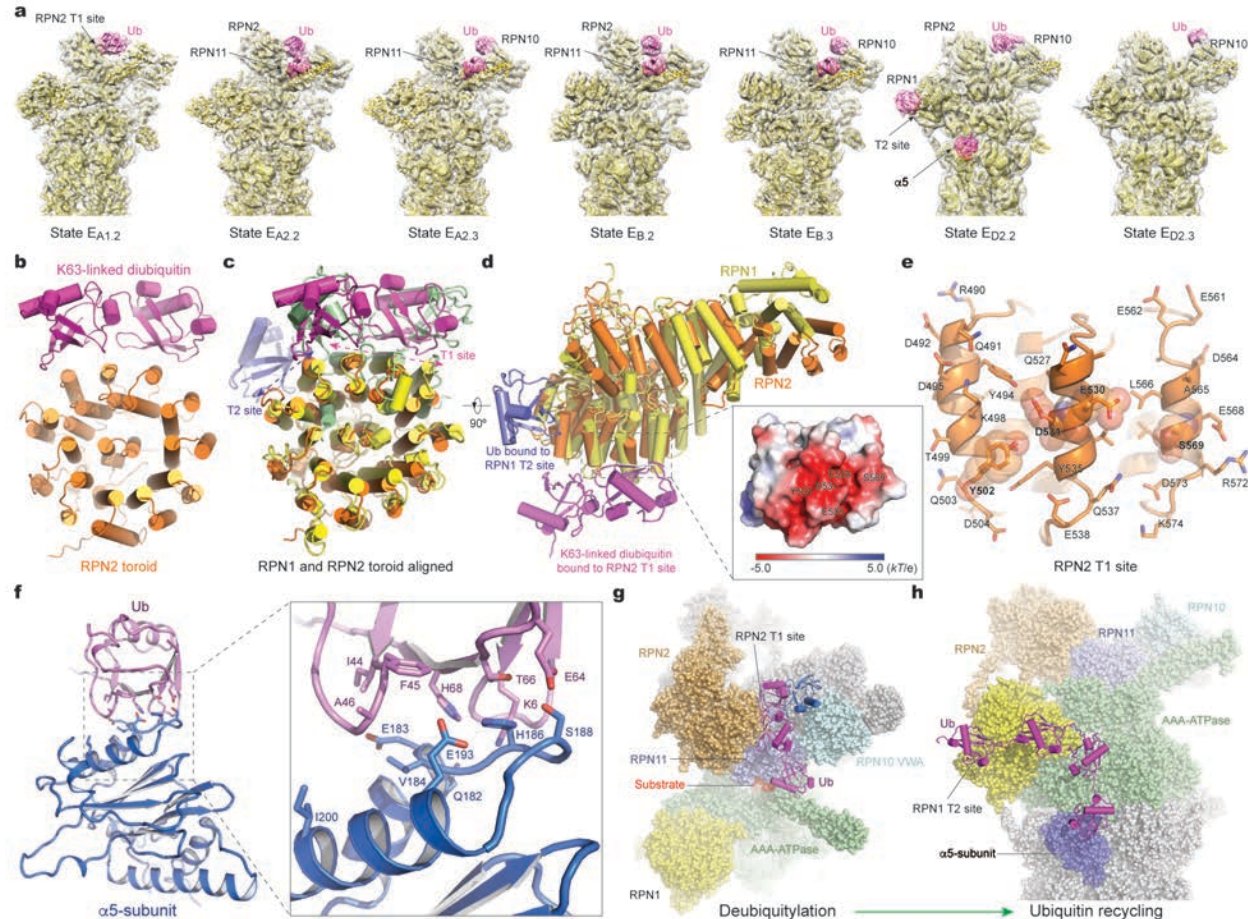


551 **Figure 2. Performance evaluation of AlphaCryo4D for sub-3-Å reconstructions of**
552 **conformational continuum. a-c**, Plots of 3D classification precisions of the 20 NLRP3
553 conformers from blind assessments on the simulated NLRP3 dataset with SNR of 0.01, using
554 AlphaCryo4D (**a**), PCA-based clustering implemented in CryoSPARC (**b**) and 3D maximum-
555 likelihood (ML3D) method implemented in RELION (**c**). All 3D conformers in panel (a) were
556 reconstructed to 2.6-2.9 Å resolution (Extended Data Fig. 3m). Asterisks mark the missing
557 conformers that were completely lost due to misclassification by PCA and ML3D. **d-f**, Typical
558 side-by-side comparison of density map quality and local resolution of the same conformer (ID
559 6) reconstructed by AlphaCryo4D (**d**), PCA in CryoSPARC (**e**) and ML3D in RELION (**f**). The
560 maps are colored by their local resolutions calculated by Bsoft blocres program. **g-i**, Closeup
561 side-by-side comparison of the same two secondary structures, including a loop (upper row) and
562 a helix (lower row), in the NACHT domain illustrates considerable improvements in local
563 density quality and resolution by AlphaCryo4D (**g**) as opposed to PCA/CryoSPARC (**h**) and
564 ML3D/RELION (**i**). The locations of the loop and helix in the NLRP3 structure are marked by
565 dashed boxes in panel (**f**). The same ground-truth atomic model of Conformer 6 shown in stick
566 representations is superimposed with the density maps shown in blue mesh representations, all
567 from the same perspective. The atomic model was not further refined against each map for visual
568 validation of the map accuracy.

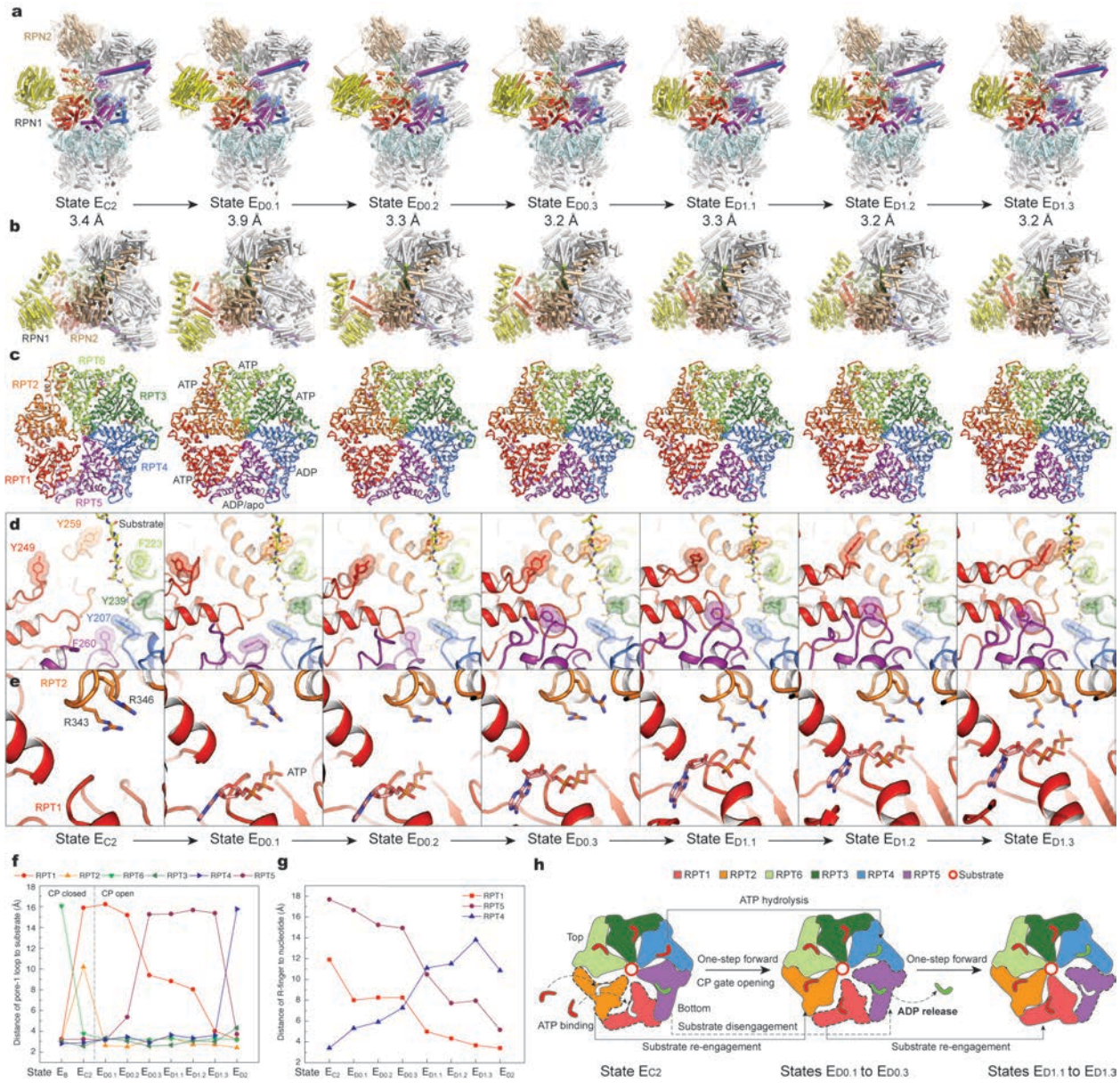


570

571 **Figure 3. Energetic differences of the singly and doubly capped proteasomes. a-c,** Free-energy
 572 landscapes of the substrate-free ATPγS-bound 26S proteasome (**a**), the substrate-engaged singly
 573 capped (SC) proteasome (**b**), and the substrate-engaged doubly capped (DC) proteasomes (**c**)
 574 computed by AlphaCryo4D. 19 conformational states of the RP-CP subcomplex are marked on
 575 the energy landscape. **d**, Comparison of the state distribution of RP in the SC and DC
 576 proteasomes. **e**, State distribution matrix of the DC proteasome obtained using AlphaCryo4D on
 577 experimental data, colored by the particle numbers in the DC states, with the horizontal and
 578 vertical axes representing the states of two RPs bound to the same CP. **f**, State distribution matrix
 579 of the DC proteasome predicted by a control model assuming that the two RPs in the same DC
 580 proteasome are completely independent of each other or uncoupled. The model assumes the
 581 same total number of DC particles and the same probability of observing each RP state as
 582 experimentally measured. **g**, State distribution difference matrix of the DC proteasome by
 583 experimental results minus the model predictions assuming uncoupled two RPs, colored by the
 584 absolute particle number difference. **h**, Relative differences of the DC proteasome in unit of
 585 percentage. The relative difference is the ratio of absolute difference divided by the particle
 586 numbers from the model prediction in each DC state.



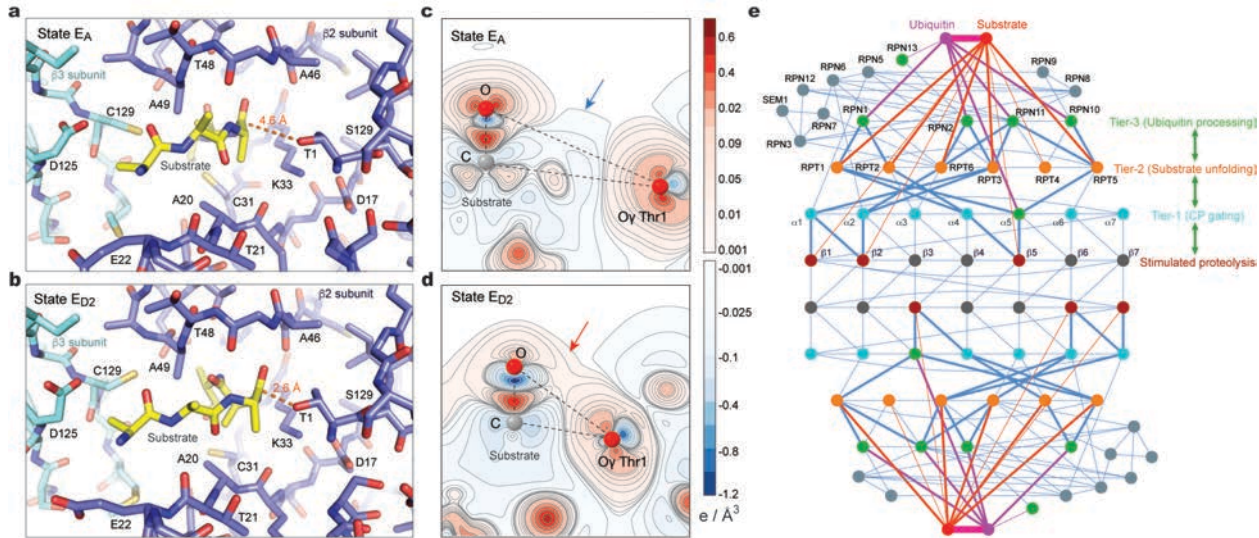
602 subunit structures are aligned together and viewed from a perspective that is rotated 90° relative
603 to the orientation in panel **(c)**, showing that the two subunits are structurally homologous. Insert,
604 electrostatic surface of the RPN2 T1 site showing its acidic nature. **e**, Closeup view of the RPN2
605 T1 site composed of three helices in cartoon representation with the side chains shown in stick
606 representation. The key residues contacting ubiquitin are highlighted with transparent sphere
607 representation. **f**, Structure of ubiquitin-bound α 5 subunit shown in cartoon representation. The
608 side chains of residues involved in the intermolecular interactions are shown in stick
609 representation and are zoomed in on the right. **g**, A Lys63-linked triubiquitin chain model fitted
610 from the cryo-EM maps of states $E_{A2.2}$ and $E_{B.2}$ is shown in purple cartoon representation and
611 spans from the RPN2 T1 site to the RPN11 deubiquitylation site. The RPN10 VWA-bound
612 monoubiquitin fitted in states $E_{A2.3}$ and $E_{B.3}$ is superimposed in blue cartoon representation. The
613 proteasome is shown as space-filling sphere representations. **h**, A Lys63-linked tetraubiquitin
614 chain model derived from the cryo-EM map of state $E_{D2.2}$. The two terminal ubiquitin molecules
615 are fitted from their highest-resolution cryo-EM densities available at the RPN1 T2 and α 5-
616 subunit sites, whereas the middle two molecules are hypothetically modelled.



617

618 **Figure 5. Single-nucleotide exchange dynamics of the AAA-ATPase motor.** **a**, Side views of
619 the substate-engaged RP-CP subcomplex in seven sequential conformers between states E_{C2} and
620 $E_{D1.3}$, as shown in cartoon representation and with only half CP shown. **b**, Top views of the
621 seven sequential conformers, showing the overall lid rotation and the relative rotation between
622 RPN1 and the rest of the RP structure. **c**, The substrate-bound AAA-ATPase structures of the
623 seven conformers in cartoon representations. The substrates and nucleotides are shown in stick
624 representations. **d**, Close-up views of the pore-1 loop interactions with the substrate (in yellow
625 stick representation), with the aromatic residues in the pore-1 loops highlighted by transparent
626 sphere representations. The seven snapshots show that the RPT1 pore-1 loop is gradually moved

627 to a position in direct contact with the substrate, whereas the RPT5 pore-1 loop is gradually
628 moved away from the substrate and flipped up and out. **e**, Close-up views of the RPT1
629 nucleotide-binding sites in different states, showing its gradual closeup by the R-fingers from
630 RPT2. **f**, Plots of distances of the pore-1 loops of all RPT subunits to the substrate measured in
631 the atomic structures of 9 sequential conformational states. **g**, Plots of distances of R-finger to
632 the nucleotides bound to three RPT subunits measured in the atomic structures of 8 sequential
633 conformational states. **h**, Schematic illustrating the ATP hydrolysis reaction and nucleotide
634 exchange associated with the intermediates during the transition from state E_{C2} to E_{D1.3}.
635
636



637

638 **Figure 6. Hierarchical allosteric regulation of proteasome activity.** **a** and **b**, Structure of the
639 catalytic site with a substrate polypeptide bound at residue Thr1 in the β_2 subunit of the CP in
640 the closed-gate state EA at 2.7- \AA resolution (**a**) and in the open-gate state ED2 at 2.5- \AA resolution
641 (**b**). **c** and **d**, Charge density difference contour maps at the proteolytic active site of the β_2
642 subunit computed by the quantum mechanical DFT based on the atomic structures of states EA
643 (**c**) and ED2 (**d**). The contours are plotted in the plane passing through the Thr1-Oy atom and the
644 nearest carbonyl carbon and oxygen atoms of the substrate. The interactions of the Thr1-Oy atom
645 and the carbonyl group lead to the nucleophilic attack as the first step of the proteolytic process.
646 Due to the proximity shown in (**b**), a bonding interaction starts to form in the ED2 states,
647 indicated by the slight positive charge difference region (red arrow), whereas there is no such
648 region formed in the EA state and the pair is well separated by a non-bonding charge depletion
649 region (blue arrow). **e**, An interactome network diagram of the proteasome illustrating the grand
650 allosteric regulation model and highlighting the key inter-subunit interaction pathways for
651 proteasome autoregulation. The base subunits hosting ubiquitin-binding sites and the
652 deubiquitinase RPN11 are shown as the green nodes; the AAA-ATPase subunits as the orange
653 nodes; the α -type subunits as the cyan nodes; the catalytically active β_1, β_2 and β_5 subunits as
654 the crimson nodes. Steel blue lines represent inter-subunit interactions; purple lines represent the
655 interactions with ubiquitin; and red lines represent substrate polypeptide interactions. Bold lines
656 highlight the shortest pathways connecting the three tiers of regulatory subunits that are expected
657 to propagate the allosteric regulation from ubiquitin interactions down to the six proteolytic

658 active sites in the CP. The network diagram is constructed according to all 64 structural models
659 of the substrate-bound proteasome in this study.
660

661 **Methods**

662 **Overall procedure of AlphaCryo4D**

663 The design of AlphaCryo4D follows a few key ideas and objectives. First of all, we expect to
664 maximally use all available particles and make particle selection via comprehensive, objective
665 criteria such as the reproducibility and robustness in deep-learning-based classification. To this
666 end, we minimize any substantial manual particle rejection before entering the steps of
667 AlphaCryo4D and avoid any subjective particle selection within the AlphaCryo4D procedure.
668 Next, we expect to devise an automated procedure to examine the robustness of 3D classification
669 at single-particle level. We consider that any objective functions in image similarity
670 measurement suffer from certain degree of errors in particle alignment that often lead to a greater
671 degree of misalignment with decreasing the signal-to-noise ratio (SNR). Thus, we expect to
672 devise an integrative procedure in which each particle is analyzed for at least three times to
673 examine the robustness of the 3D classification algorithm with respect to individual particles. We
674 wish to keep particle images that exhibits greater robustness during data processing. Thus, within
675 the entire AlphaCryo4D procedure, the only way to reject particles is via the energy-based
676 particle voting algorithm that is completely objective.

677 In practice, AlphaCryo4D consists of four major steps (Fig. 1a). First, all single-particle
678 images are randomly divided into $M+1$ groups of equal data sizes. In the step called ‘particle
679 shuffling’, one group of particles is taken out of the dataset to form a shuffled dataset. This
680 procedure is repeated for $M + 1$ times, each time with a different particle group being taken out,
681 resulting in $M + 1$ shuffled datasets (Extended Data Fig. 1). Each shuffled dataset is subject to
682 3D volume bootstrapping separately. In each case, all particles in a shuffled dataset are aligned
683 in a common frame of reference through a consensus 3D refinement, and then clustered into tens
684 to hundreds of 3D reconstructions through Bayesian clustering, which ensures that only
685 structurally similar particles are clustered into the same 3D volumes. In total, thousands of
686 volumes from all shuffled datasets are expected to be bootstrapped through these steps. As a
687 result, each particle image is used in 3D reconstructions of M different volumes after particle
688 shuffling and volume bootstrapping. Second, all bootstrapped volumes are learnt by an
689 autoencoder based on a deep residual convolutional neural network in an unsupervised
690 fashion^{3,20} (Fig. 1b, Extended Data Table 1). A 3D feature map is extracted for each volume and
691 is juxtaposed with the volume data for nonlinear dimensionality reduction by manifold

embedding with t-distributed stochastic neighbor embedding (t-SNE) algorithm⁴. Third, the learnt manifold is then used to compute a free-energy landscape via the Boltzmann distribution⁵. A string method is used to search the minimum energy path (MEP) on the learnt free-energy landscape^{21,22}. The local energy minima or the transition states connecting can be defined as the centers of 3D clustering, with a circular range defined as cluster boundaries for subsequent particle voting. Forth, because each particle is used M times during volume bootstrapping, it is mapped to M locations on the free-energy landscape. The mapping of each copy of the particle is called a ‘vote’. By counting the number of votes of the same particle being mapped within the same cluster boundary on the energy landscape, we can evaluate the reproducibility of manifold learning at single-particle level. Each particle is classified to the 3D cluster that receives more than $M/2$ votes of this particle. If none of the 3D clusters on the energy landscape receives more than $M/2$ votes of a given particle, the corresponding particle is voted out in the procedure and is excluded for further 3D reconstruction. As a result, each of the final 3D reconstructions includes structurally homogeneous particles that can potentially achieve higher resolution.

AlphaCryo4D exhibits several advantages as well as certain limitation. First, it allows a maximal number of particles to be assessed and classified in an integrative procedure based on uniform, objective criteria, such as their reproducibility and robustness in deep learning. Second, the energy-based particle-voting algorithm can potentially rescue certain particles that are prone to be misclassified if processed only once, thus boosting the efficiency of particle usage without necessarily sacrificing quality and homogeneity of selected particles. Third, the use of energy landscape to direct 3D clustering of conformational states has an intuitive physical meaning and allows users to examine kinetic relationships between the adjacent states at the same time of conducting 3D classification and to potentially discover new conformations. All these advantages are well demonstrated in our analysis of both simulated and experimental datasets. The limitation of AlphaCryo4D lies in that it requires generally larger datasets and more computational costs to fully exploit its advantages. We do not expect to achieve considerably better results for a small dataset. Moreover, its outcomes are dependent on the success of initial consensus alignment of all particles during the first step of particle shuffling and volume bootstrapping. Failure in obtaining accurate alignment parameters can lead to futile, erroneous, nonsensical classification in the subsequent steps.

722 Particle shuffling for bootstrapping 3D volumes

723 A key philosophy of the AlphaCryo4D design is to avoid subjective judgement on the particle
724 quality and usability as long as it is not apparent junks like ice contaminants, carbon edge and
725 other obvious impurities. A deep-learning-based particle picking in DeepEM⁴⁴, Torpaz⁴⁵ or other
726 similarly performed software is favored for data preprocessing prior to AlphaCryo4D. To
727 prepare particle datasets for AlphaCryo4D, an initial unsupervised 2D image classification and
728 particle selection, preferentially conducted by the statistical manifold-learning-based algorithm
729 in ROME¹⁷, is necessary to ensure that no apparent junks are selected for further analysis and
730 that the data have been collected under an optimal microscope alignment condition, such as
731 optimized coma-free alignment. No particles should be discarded based on their structural
732 appearance during this step if they are not apparent junks. Any additional 3D classification
733 should be avoided to pre-maturely reject particles prior to particle shuffling and volume
734 bootstrapping in the first step of AlphaCryo4D processing. Pre-maturely rejecting true particles
735 via any 2D and 3D classification is expected to introduce subjective bias and to impair the native
736 conformational continuity and statistical integrity intrinsically existing in the dataset.

737 In raw cryo-EM data, 2D transmission images of biological macromolecules suffer from
738 extremely heavy background noise, due to the use of low electron dose to avoid radiation
739 damage. To tackle the conformational heterogeneity of the protein sample of interest in the
740 presence of heavy image noise, we devised the particle shuffling and volume bootstrapping
741 procedure that incorporates the Bayesian or maximum-likelihood-based 3D clustering⁸. To
742 enable the particle-voting algorithm in the late stage of AlphaCryo4D, each particle is reused M
743 times during particle shuffling to bootstrap a large number of 3D volumes (Extended Data Fig.
744 1a). First, all particle images are aligned to the same frame of reference in a consensus 3D
745 reconstruction and refinement in RELION⁸ or ROME to obtain the initial alignment parameters
746 of three Euler angles and two translational shifts. Optimization for high alignment accuracy in
747 this step must be pursued to make the volume bootstrapping more efficient and to avoid the error
748 propagation to the subsequent steps in AlphaCryo4D. Thus, coarsely classifying the dataset
749 during image alignment, restricting the 3D alignment to a moderate resolution like 10 Å or 15 Å
750 for global parameter search, progressing to small enough angular steps in the final stage of
751 consensus refinement, must be appropriately practiced in order to optimize the initial 3D
752 alignment of all particles. Failure of initial alignment of particles would lead to failure of all
753 subsequent AlphaCryo4D analysis.

754 Next, based on the results of consensus alignment, in the particle-shuffling step, all particles
755 were divided into $M + 1$ groups, and M was set to an odd number of at least 3. Then the whole
756 dataset was shuffled $M + 1$ times by removing a different group out of the dataset each time.
757 Each shuffled dataset is classified into a large number of 3D volumes, often several hundreds, by
758 the maximum-likelihood classification algorithm without further image alignment in RELION.
759 This step is repeated $M + 1$ times, each time on a shuffled dataset missing a different group
760 among the $M + 1$ groups. Due to the effect of M -fold data augmentation and enhancement by
761 particle shuffling, the outcome of this entire process is expected to bootstrap up to thousands of
762 3D volumes in total. Each particle is used and contributed to the 3D reconstructions of M
763 volumes, which prepare it for the particle-voting algorithm to evaluate the robustness and
764 reproducibility of each particle with respect to the deep learning-based 3D classification later.

765 For processing a large dataset including millions of single-particle images, it becomes
766 infeasible even for a modern high-performance computing system to do the consensus alignment
767 by including all particles once in a single run due to limitation of supercomputer memory and the
768 scalability of the alignment software such as RELION or ROME, although ROME has been
769 specifically optimized for its scalability on CPU-based supercomputing cluster¹⁷ and RELION
770 has been optimized for GPU-based cluster⁹. To tackle this issue, the whole dataset is randomly
771 split into a number of sub-datasets for batch processing, with each sub-dataset including about
772 one to two hundred thousand particles, depending on the scale of available supercomputing
773 system. This strategy can substantially reduce the supercomputer memory pressure and
774 requirement. In each sub-dataset, all particles were divided into $M + 1$ groups and subject to the
775 particle shuffling and volume bootstrapping procedure as described above. To balance the
776 computational cost and algorithmic efficiency, we used $M = 3$ in the entire data processing
777 workflow involved in the current study, implying that every particle was used three times for
778 subsequent computation before particle voting. But a higher M value might be beneficial for
779 smaller dataset or lower signal-to-noise ratio, whose effects are not investigated in the present
780 study due to the limit of computational resources and feasibility.

781 **Deep residual autoencoder for 3D feature extraction**

782 To extract the deep 3D features of the bootstrapped volume data in an unsupervised manner, a
783 3D autoencoder was constructed using a deep Fully Convolutional Network (FCN) composed of
784 residual blocks^{3,20}. The structure of the 3D autoencoder consists of the encoder and the decoder,

785 which are denoted as \mathcal{E} and \mathcal{D} , respectively (Fig. 1b, Extended Data Table 1). The relation
786 between the output \mathbf{y} and the input \mathbf{x} of the network can be expressed as:

787
$$\mathbf{y} = \mathcal{D}(\mathcal{E}(\mathbf{x})), \quad (1)$$

788 in which \mathbf{x} is the input 3D density volume with the size of N^3 , where N is the box size of the
789 density map in a unit of pixels. For reconstruction of the 3D volumes and further optimization,
790 the decoding output \mathbf{y} should be in the same size and range with the input data \mathbf{x} . In this way, the
791 framework of FCN is established to restore the input volume, using the sigmoid function $S(x) =$
792
$$\frac{1}{1+\exp(-x)}$$
 as the activation function of the decoding layer to normalize the value of \mathbf{y} into the
793 range (0, 1). Meanwhile, all 3D density maps \mathbf{x} should be preprocessed as the function (2) before
794 inputted to the deep neural network:

795
$$x_{ijk} := \frac{x_{ijk} - x_{min}}{x_{max} - x_{min}}, \quad i, j, k = 1, 2, \dots, N. \quad (2)$$

796 where x_{min} and x_{max} are, respectively, the minimum and minimax value in all x_{ijk} .

797 The distance between the decoded maps and the input volumes can be used for constructing
798 the loss function to train the 3D kernels and bias of the networks. The value distribution of the
799 encoded 3D feature maps $\mathbf{z} = \mathcal{E}(\mathbf{x})$ is expected to be an abstract, numerical representation of the
800 underlying structures in the volume data, which may not necessarily have any intuitive real-space
801 physical meanings. The neural network is capable of extracting such abstract information in the
802 prediction step, with no restriction on the feature maps \mathbf{z} in the expression of training loss. The
803 loss function is then formulated as:

804
$$L(\boldsymbol{\theta}; \mathbf{x}, \mathbf{y}) = \frac{1}{N^3} \sum_{i,j,k=1}^N \|x_{ijk} - y_{ijk}\|^2 + \lambda \|\boldsymbol{\theta}\|^2, \quad (3)$$

805 where $\boldsymbol{\theta}$ denotes the weights and bias of the network, and λ is L2 norm regularization
806 coefficient. As the feature of the complex structure is difficult to be learnt from the 3D volume
807 data, the value of λ is generally set to 0 to focus on the first term of the expression (3) unless
808 overfitting arises.

809 To improve the learning capacity of the 3D autoencoder, residual learning blocks containing
810 3D convolution and transpose convolution layers are employed in the encoder and decoder,
811 respectively. In each residual block, a convolution/transpose convolution layer followed by
812 Batch Normalization (BN) layer and activation layer appears twice as a basic mapping, then

813 adding with the input to generate the output. The mathematical expression of the l th block can be
814 shown as:

815

$$\begin{cases} \mathbf{y}_l = \mathcal{F}(\mathbf{x}_l; \boldsymbol{\theta}_l) + \mathbf{x}_l \\ \mathcal{F}(\mathbf{x}_l; \boldsymbol{\theta}_l) = \mathcal{C}(\mathcal{C}(\mathbf{x}_l)), \quad (4) \\ \mathcal{C}(\mathbf{x}_l) = a(b(c(\mathbf{x}_l))) \end{cases}$$

816 where \mathbf{x}_l and \mathbf{y}_l represent the input and the output of this block, respectively. $\mathcal{F}(\mathbf{x}_l; \boldsymbol{\theta}_l)$ denotes
817 the basic mapping of the l th block parameterized by $\boldsymbol{\theta}_l$, and $\mathcal{C}(\mathbf{x}_l)$ is the sequential operation of
818 convolution/transpose convolution c , BN b and activation a . The rectified linear unit (ReLU)
819 function is used in all the activation layers but the last one. In addition, the function (4) demands
820 that the output of mapping function $\mathcal{F}(\mathbf{x}_l; \boldsymbol{\theta}_l)$ must have the same dimension as the input \mathbf{x}_l . If
821 this is not the case, the input \mathbf{x}_l must be rescaled along with $\mathcal{F}(\mathbf{x}_l; \boldsymbol{\theta}_l)$ using a
822 convolution/transpose convolution transformation $c'(\mathbf{x}_l)$ with an appropriate stride value, the
823 parameters of which can be updated in the training step.

824 To analyze a large number of volumes, training of the autoencoder neural network should be
825 treated elaborately to obtain suitable kernels and bias. First of all, parallel computation with
826 multiple GPUs must be implemented to reduce the training time. Then the parameters of the
827 network are optimized by the stochastic gradient descent Adam (Adaptive moment estimation)
828 algorithm, in which the gradients of the objective function $L(\boldsymbol{\theta}; \mathbf{x}, \mathbf{y})$ with respect to the
829 parameters $\boldsymbol{\theta}$ can be calculated by the chain rule. Moreover, the learning rate will be reduced to
830 one tenth if the loss function does not decrease in three epochs based on the initial value of 0.01.
831 After trained about 50 epochs, the best model is picked to execute the task of structural feature
832 extraction. Using the unsupervised 3D autoencoder, the feature maps $\mathbf{z} = \mathcal{E}(\mathbf{x})$ encoding the
833 structural discrepancy among the 3D volume data can be extracted automatically without any
834 human intervention.

835 **Manifold embedding of free energy landscape**

836 To prepare for the energy landscape reconstitution, each bootstrapped 3D volume was
837 juxtaposed with its 3D feature map learnt by the autoencoder to form an expanded higher-
838 dimensional data point. All the expanded data points were then embedded onto a low-
839 dimensional manifold via the t-SNE algorithm by preserving the geodesic relationships among
840 all high-dimensional data⁴. During manifold embedding, it is assumed that the pairwise
841 similarities in the high dimensional data space and low dimensional latent space follow a

842 Gaussian distribution and a Student's t-distribution, respectively, which can be formulated as:

843

$$\begin{cases} p_{ij} = \frac{\exp(-\|\mathbf{x}_i - \mathbf{x}_j\|^2/2\sigma_i^2)}{\sum_{i \neq j} \exp(-\|\mathbf{x}_i - \mathbf{x}_j\|^2/2\sigma_i^2)}, & i \neq j \\ q_{ij} = \frac{(1 + \|\mathbf{y}_i - \mathbf{y}_j\|^2)^{-1}}{\sum_{i \neq j} (1 + \|\mathbf{y}_i - \mathbf{y}_j\|^2)^{-1}}, & i \neq j \end{cases} \quad (5)$$

844 where p_{ij} and q_{ij} represent the similarity distributions in the high and low dimensional spaces,
845 \mathbf{x}_k and \mathbf{y}_k ($k = i, j$) are the data points of the high and low dimensional spaces, respectively. The
846 parameter σ^2 is the variance of the Gaussian distribution. In addition, p_{ii} and q_{ii} are both set to
847 zero to satisfy the constraint of symmetry.

848 To find the value y_k of each data point, an objective function measuring the distance between
849 the similarity distribution p_{ij} and q_{ij} had to be well defined. Here the relative entropy, also
850 called the Kullback-Leibler (KL) divergence,

851

$$KL(P \parallel Q) = \sum_{i,j} p_{ij} \log \frac{p_{ij}}{q_{ij}}, \quad (6)$$

852 was employed and minimized by the gradient descent algorithm with the momentum method⁴⁶.

853 After the manifold embedding by t-SNR, each 3D volume is mapped to a low-dimensional
854 data point in the learnt manifold. The coordinate system, in which the low-dimensional
855 representation of the learnt manifold is embedded, is used for reconstructing and visualizing the
856 free energy landscape. In accordance with the Boltzmann distribution, the free energy of each
857 data point in the low-dimensional space can be estimated using the particle number included in
858 the original 3D volume corresponding to each low-dimensional data point on the manifold:

859

$$\Delta\Delta G_i = -k_B T \ln \frac{N_i}{\sum_i N_i}, \quad (7)$$

860 where $\Delta\Delta G_i$ denotes the free energy difference of the data point with the particle number of N_i
861 against a common reference energy level, k_B is the Boltzmann constant and T is the temperature
862 in Kelvin. The free energy landscape was plotted by interpolation of the free energy difference in
863 areas with sparse data.

864 Minimum energy path finding using the string method

865 The string method is an effective algorithm to find the minimum energy path (MEP) on the
866 potential energy surface²¹. To extract the dynamic information implicated in the experimental
867 free energy landscape, an improved and simplified version of the string method was developed to

868 search the possible state-transition pathway or MEP²². Along the MEP on the learnt energy
869 landscape, the local minima of interest could be defined as 3D clustering centers to guide the
870 particle-voting algorithm for 3D classification, on the basis of which particles of the same
871 conformation could be clustered to generate high-resolution cryo-EM density maps (Extended
872 Data Fig. 1b). The objective of the MEP identification in barrier-crossing events lies in finding a
873 curve γ having the same tangent direction as the gradient of free energy surface ∇G . It can be
874 expressed as:

875
$$(\nabla G)^\perp(\gamma) = 0, \quad (8)$$

876 where $(\nabla G)^\perp$ denotes the component of ∇G perpendicular to the path γ . To approach the
877 objective function (4), two computational steps, named evolution of the images and
878 reparameterization of the string, are iterated until convergence within a given precision
879 threshold.

880 *Evolution of the images.* After initialization with the starting and ending points, the positions
881 of interval images were updated according to gradient of the free energy at the t th iteration:

882
$$\varphi_i^{*(t)} = \varphi_i^{(t-1)} - h \nabla G(\varphi_i^{(t-1)}), \quad (9)$$

883 with $\varphi_i^{(t)}$ ($i = 0, 1, \dots, N$) being the i th intermediate image at the t th iteration (* denoting the
884 temporary values), and h the learning rate.

885 *Reparameterization of the string.* The values of positions $\varphi_i^{(t)}$ ($i = 0, 1, \dots, N$) were
886 interpolated onto a uniform mesh with the constant number of points. Prior to interpolation, the
887 normalized length $\alpha_i^{*(t)}$ ($i = 0, 1, \dots, N$) along the path was calculated as:

888
$$\alpha_0^{*(t)} = 0, \quad \alpha_i^{*(t)} = \alpha_{i-1}^{*(t)} + \frac{\|\varphi_i^{*(t)} - \varphi_{i-1}^{*(t)}\|}{\sum_{i=1}^N \|\varphi_i^{*(t)} - \varphi_{i-1}^{*(t)}\|}, \quad i = 1, 2, \dots, N. \quad (10)$$

889 Given a set of data points $(\alpha_i^{*(t)}, \varphi_i^{*(t)})$, the linear interpolation function was next used to
890 generate the new values of positions $\varphi_i^{(t)}$ ($i = 0, 1, \dots, N$) at the uniform grid points $\alpha_i^{(t)}$ ($i =$
891 $0, 1, \dots, N$). The iteration was terminated when the relative difference $\sum_{i=0}^N \|\varphi_i^{(t)} - \varphi_i^{(t-1)}\|^2 / N$
892 became small enough.

893 Energy-based particle voting algorithm

894 The particle-voting algorithm was designed to conduct 3D classification, particle quality control,
895 reproducibility test and particle selection in an integrative manner. The particle-voting algorithm

896 mainly involves two steps (Extended Data Fig. 1b). First, we count the number of votes for each
897 particle mapped within the voting boundaries of all 3D clusters on the free-energy landscape.
898 One vote is rigorously mapped to one copy of the particle used in reconstructing a 3D volume
899 and to no more than one 3D cluster on the energy landscape where the corresponding volume is
900 located. Thus, each particle can have M votes casted for no more than M 3D clusters. If the vote
901 is mapped outside of any 3D cluster boundary, it becomes an ‘empty vote’ with no cluster label.
902 Each non-empty vote is thus labeled for both its particle identify and corresponding cluster
903 identify. For each pair of particle and cluster, we compute the total number (K) of votes that the
904 cluster receives from the same particle. Each particle is then assigned and classified to the 3D
905 cluster that receives $K > M/2$ votes from this particle (Extended Data Fig. 1b). Note that after
906 particle voting, each particle is assigned no more than once to a 3D class, with its redundant
907 particle copies removed from this class. This strategy only retains the particles that can
908 reproducibly vote for a 3D cluster corresponding to a homogeneous conformation, while
909 abandoning those non-reproducible particles with divergent, inconsistent votes.

910 Because the particle-voting algorithm imposes strong constraints on the numeric performance
911 of particles in deep learning, it could lead to particle number insufficiency in the cases of smaller
912 but potentially interested 3D classes. To remedy this limitation, an alternative, distance-based
913 classification algorithm was devised to replace the particle-voting algorithm when there are not
914 enough particles to gain the advantage of particle voting (Extended Data Fig. 1c). In this method,
915 the distances of all M copies of each particle to all 3D cluster centers on the energy landscape are
916 measured and ranked. Then, the particle is classified to the 3D cluster of the shortest distance. A
917 threshold could also be manually preset to remove particles that are too far away from any of the
918 cluster centers. The distance-based classification method can keep more particles, but it ignores
919 the potential issue of irreproducibility of low-quality particles. Thus, it is proven to be less
920 accurate in 3D classification (Extended Data Fig. 5d, i, n). In other words, it trades off the
921 classification accuracy and class homogeneity to gain more particles, which is expected to be
922 potentially useful for small datasets or small classes. By contrast, the energy-based particle-
923 voting algorithm imposes a more stringent constraint to select particles of high reproducibility
924 during classification, resulting in higher quality and homogeneity in the classified particles,
925 which is superior to the distance-based classification method (Extended Data Fig. 5e, j, o).

926 **Data-processing workflow of AlphaCryo4D**

- 927 Input: single-particle cryo-EM dataset after initial particle rejection of apparent junks.
928 Output: free energy landscape, MEP, 3D class assignment of each particle and high-resolution
929 density maps.
- 930 1. Bootstrap a large number of 3D volumes through particle shuffling, consensus alignment and
931 Bayesian classification.
- 932 a. Split the particles dataset randomly to many sub-datasets, if necessary, for batch
933 processing of particle shuffling and volume bootstrapping.
- 934 b. For each sub-dataset, conduct consensus alignment to generate initial parameters
935 of Euler angles and translations.
- 936 c. Divide each sub-dataset into $M + 1$ groups, shuffle the sub-dataset $M + 1$ times
937 and each time take a different group out of the shuffled sub-dataset, giving rise to
938 $M + 1$ shuffled sub-datasets all with different collection of particles.
- 939 d. Conduct 3D Bayesian classification on all the $M + 1$ shuffled sub-datasets to
940 generate hundreds of 3D volumes, making each particle to contribute to M
941 different volumes.
- 942 e. Repeat steps (b) to (d) for all sub-datasets.
- 943 2. Extract deep features of all volume data with the 3D deep residual autoencoder.
- 944 a. Initialize the hyper-parameters of the 3D autoencoder in Table 1.
- 945 b. Train this neural network with the 3D volume data to minimize mean square error
946 between the decoding layer and the input by the Adam algorithm of initial
947 learning rate 0.01.
- 948 c. Extract the feature maps of all volumes from the encoding layer.
- 949 3. Embed the volume data to low-dimensional manifolds through the t-SNE algorithm and
950 compute the free-energy landscape.
- 951 a. Calculate the pairwise similarities between volumes using their feature-map-
952 expanded volume vectors, and randomly initialize the low-dimensional points.
- 953 b. Minimize the KL divergence by the Momentum algorithm to generate the low-
954 dimensional embeddings.
- 955 c. Compute the free energy landscape with the low-dimensional coordinates.
- 956 4. Apply the string method to find the MEP on the free energy landscape, along which 3D
957 density maps of the same conformation are clustered together.

- 958 a. Initialize the transition path with a straight line between the given starting and
959 ending points.
960 b. Update the transition path according to Equations (9) and (10) until it converges
961 to the expected MEP.
962 c. Sample the clustering centers along the MEP and calculate the recommended
963 clustering radius.
964 5. Classify all particles through the energy-based particle-voting algorithm.
965 a. Define the local energy minima as the 3D clustering centers and their
966 corresponding cluster boundary for particle voting.
967 b. For each particle, cast a labelled vote for a 3D cluster when a volume containing
968 one of the M particle copies is located in the voting boundary of the 3D cluster.
969 c. Count the number of votes of each particle with respect to each 3D cluster and
970 assign the particle to the 3D cluster that receives more than $M/2$ votes from this
971 particle.
972 6. Refine the 3D density maps to high resolution using particles classified into the same 3D
973 classes.

974 **Blind assessments using simulated datasets**

975 Three simulated datasets with the SNRs of 0.05, 0.01 and 0.005 were employed to benchmark
976 AlphaCryo4D and to compare its performance with conventional methods. Particles were
977 computationally simulated by projecting the 20 3D density maps calculated from 20 hypothetical
978 atomic models emulating continuous rotation of the NLRP3 inflammasome protein. The 20
979 atomic models were interpolated between the inactive NLRP3 structure and its hypothetical
980 active state, which was generated through homology modeling using the activated NLRC4
981 structure²³. The 20 atomic models represent sequential intermediate conformations during a
982 continuous rotation in its NATCH domain against its LRR domain over an angular range of 90°.
983 Each conformation is thus rotated 4.5° over its immediate predecessor in the conformational
984 continuum sequence. 100,000 simulated particle images per conformational state were generated
985 with random defocus values in range of -0.5 to -3.0 μm , resulting in 2 million particles for each
986 dataset of a given SNR. The pixel size of the simulated image was set to the same as the pixel
987 size (0.84 Å) of the real experimental dataset of NLRP3-NEK7 complex. To emulate realistic
988 circumstances in cryo-EM imaging, Gaussian noises, random Euler angles covering half a sphere

989 and random in-plane translational shifts from -5.0 to 5.0 pixels were then added to every particle
990 image.

991 Each of the three simulated heterogeneous NLRP3 datasets of three different SNRs were
992 analyzed separately by AlphaCryo4D and used to characterize the performance and robustness of
993 AlphaCryo4D against the variation of SNR. In the step of particle shuffling and volume
994 bootstrapping, 2,000,000 particles in the dataset of any given SNR were divided randomly into
995 10 sub-datasets for batch processing. The orientation of each particle was determined in the
996 initial 3D consensus alignment in RELION, which did not change in the subsequent 3D
997 classification. In this step, the maximum number of iterations of the 3D alignment was set up as
998 30, with the initial reference low-pass filtered to 60 Å. 3-fold particle shuffling (indicated as $\times 3$
999 below) was conducted on each sub-dataset for volume bootstrapping. The first round of
1000 maximum-likelihood 3D classification divided the input shuffled particle sub-dataset into 5
1001 classes, each of these classes were then further classified into 8 classes. This procedure was
1002 repeated on all shuffled particle sub-datasets. The particle shuffling and volume bootstrapping
1003 generated 1,372, 1,489, and 1,587 volumes by the datasets with SNRs of 0.05, 0.01 and 0.005,
1004 respectively. These volume data were used as inputs for deep residual autoencoder to compute
1005 low-dimensional manifolds and free-energy landscapes (Fig. 1d-f, Extended Data Fig. 2a, b).
1006 After searching the MEP on the energy landscapes by the string method, 20 cluster centers along
1007 the MEP were defined by the local energy minimum along the MEP that represent potentially
1008 different conformations of the molecule (Extended Data Fig. 2a-c). The particle-voting algorithm
1009 was applied in every cluster to determine the final particle sets for all 3D classes. For the purpose
1010 of validation of the methodology and investigation of 3D classification improvement, we labeled
1011 each bootstrapped 3D volume with the conformational state that held the maximum proportion of
1012 particles in the class and computed its 3D classification precision as the ratio of the particle
1013 number belonging to the labelled class versus the total particle number in the volume (Fig. 1d,
1014 Extended Data Fig. 2a, b). Moreover, 3D classification precision and its statistical distribution
1015 among the bootstrapped data calculated from the ground truths were recorded in the intermediate
1016 steps of AlphaCryo4D, including the particle shuffling and volume bootstrapping, setup of
1017 voting boundary on the free energy landscape, distance-based 3D clustering and energy-based
1018 particle voting (Extended Data Fig. 5).

1019 To compare the classification performance of AlphaCryo4D with other methods, the ab-initio

1020 classification by 3D PCA analysis in CryoSPARC⁷ and the maximum-likelihood-based 3D
1021 (ML3D) classification in RELION^{8,9,18} had been tested on the simulated datasets. For the tests
1022 using RELION, we classified all particles directly into 20 classes and hierarchically into 4×5
1023 classes, which first divided the dataset into 4 classes, with each class further classified into five
1024 sub-classes (Extended Data Fig. 3). In the 3D PCA analysis using CryoSPARC, we first did the
1025 consensus alignment of the entire dataset to find the orientation of each particle. Then the
1026 alignment and the mask generated from the consensus alignment were used as inputs into the 3D
1027 PCA calculation, with the number of orthogonal principal modes being set to 2 in 3D
1028 classification, in consistent with the deep manifold learning algorithm. Then the 3D variability
1029 display module in the cluster mode was used to analyze the result of 3D classification. The
1030 metadata of 3D classification precisions as well as the 3D density maps from all the algorithms
1031 applied on the three simulated datasets were collected to conduct statistical analysis, as shown in
1032 Fig. 2 and Extended Data Figs. 2-5.

1033 **Computational costs of AlphaCryo4D**

1034 Although the computational cost of AlpahCryo4D is generally higher than the conventional
1035 approach, it does not appear to increase drastically and likely falls in an affordable range, while
1036 reducing the average cost of computation per conformational state. In a nutshell, we can have a
1037 brief comparison of the computational efficiency on the simulated dataset with an SNR of 0.01.
1038 In the step of 3D data bootstrapping, we split the dataset into 20 subsets, which contained
1039 100,000 particles each. The 3D consensus alignment of all 2,000,000 particles cost about 75
1040 hours using 8 V100 GPUs interconnected with the high-speed NVLink data bridge in a NVIDIA
1041 DGX-1 supercomputing system. Within each subset, the 3D Bayesian classification for one
1042 leave-one-group-out dataset cost about 2.5 hours using 320 CPUs, so the total time spent in one
1043 subset was about 10 hours using 320 CPUs in an Intel processor-based HPC cluster. In addition,
1044 it spent about 3 hours to extract feature via deep neural network using 8 V100 GPUs of the
1045 NVIDIA DGX-1 system. In contrast to about 160 hours cost in traditional classification methods,
1046 this approach cost a little more than 200 hours using 8 V100 GPUs and 320 CPUs. Taken
1047 together, these observations suggest that the computational cost and efficiency of AlphaCryo4D
1048 are within the acceptable range considering the output of more higher-resolution conformers
1049 reconstructed by these procedures.

1050 **Applications to experimental cryo-EM datasets**

1051 Three experimental cryo-EM datasets were processed using AlphaCryo4D to examine its
1052 applicability in processing real experimental cryo-EM data: (1) A small dataset of the ATP γ S-
1053 bound human proteasome¹⁵ contains only 455,680 particles, with the super-resolution pixel size
1054 of 0.685 Å. The size of ATP γ S-bound proteasome dataset was enhanced to 455,680 × 3 particles
1055 and was separated into 4 sub-datasets for volume bootstrapping. 160 volumes were bootstrapped
1056 to compute the free-energy landscape the substrate-free ATP γ S-bound proteasome (Fig. 3a). (2)
1057 The substrate-engaged human proteasome dataset² includes 3,254,352 RP-CP particles (mixed
1058 with particle images from both the DC and SC proteasomes) in total, with the physical pixel size
1059 of 1.37 Å and the box size of 300 pixels. Sample preparation, cryo-EM imaging and data
1060 collection condition as well as data pre-processing prior to 3D classification by AlphaCryo4D
1061 have been previously described in detail². To proceed with AlphaCryo4D, the whole dataset was
1062 randomly split into dozens of sub-datasets, each with 100,000 particles. Particle shuffling and
1063 volume bootstrapping procedures were repeated on each sub-dataset, which enhanced the total
1064 data size to 3,254,352 × 3 particles, and yielded 1280 volumes in total that were used to compute
1065 the free-energy landscape of the substrate-engaged proteasome (Fig. 3b, c). Particle-voting on
1066 this energy landscape detected previously missing states (such as E_{D0.2}, E_{D0.3}, E_{D1.1} and E_{D1.2}, etc.)
1067 and yielded previously determined states with improved map quality such as E_{A2} and E_{D2}.
1068 Guided by this initial discovery of new conformational states, extensive focused 3D
1069 classifications in AlphaCryo4D were performed, as described in detail in the next section, to
1070 discover novel ubiquitin-binding sites and hidden dynamics of proteasomal AAA-ATPase motor
1071 during single-nucleotide exchange. (3) The dataset of human NLRP3-NEK7 complex includes
1072 622,562 particles²³. All particles were divided into 6 sub-datasets for particle shuffling, with the
1073 total data size enhanced to 622,562 × 3 images for volume bootstrapping. Given the small
1074 molecular size of the complex, the super-resolution pixel size of 0.42 Å and the box size of 240
1075 pixels were employed in image analysis. 480 volumes were bootstrapped to compute the free-
1076 energy landscape of the NLRP3-NEK7 complex (Extended Data Fig. 4k, l). The NLRP3-NEK7
1077 dataset exhibits certain degree of orientation preference. While AlphaCryo4D was able to
1078 retrieve 3 distinct NLRP3 conformations, the resulting map resolution is limited to ~4 Å.
1079 Although this may be already an improvement over the previous analysis of this dataset by the
1080 conventional approach, the result suggests that AlphaCryo4D does not necessarily overcome the
1081 potential issues of the orientation preference.

1082 **Focused 3D classification by AlphaCryo4D**

1083 To apply AlphaCryo4D to process the experimental dataset of the substrate-engaged human 26S
1084 proteasome², a focused 3D classification protocol using AlphaCryo4D was implemented to
1085 enhance its capability in discovering transient states of extremely low particle populations and in
1086 solving highly dynamic components that may be too small to be analyzed by conventional
1087 methods^{7-9,18}. To study the local features of ubiquitin binding and substrate interactions, 3D
1088 masks corresponding to the local densities of interest were applied to all bootstrapped volume
1089 data, and the subset of interest on the free energy landscape was extracted to conduct a zoomed-
1090 in analysis. In this case, the free energy landscape calculated via masked volumes is expected to
1091 reflect the local structural variations of interest (Extended Data Fig. 6).

1092 To detect novel ubiquitin-binding sites in the proteasome, local masks were applied to focus
1093 on the features around the putative locations of ubiquitin chains. After particle shuffling for data
1094 augmentation, $732,666 \times 3$ particle images of the state E_A and E_B were utilized for computing the
1095 zoomed-in free energy landscape with 280 volumes. These particles were first aligned in a
1096 consensus alignment without any mask or resolution limit to restrict alignment parameter
1097 calculations. On the focused free energy landscape, only the region within the soft mask of the
1098 ubiquitin and its binding site was applied in the volume bootstrapping step, with the signals of
1099 the CP of the proteasome subtracted from each raw particle when dealing with the state E_A and
1100 E_B. Accordingly, the particle diameter applied in the CP subtracted proteasome was shrunk to
1101 274 Å, instead of 411 Å in the complete 26S proteasome. When the region around RPN2 masked
1102 for focused 3D classification to search for potential ubiquitin-like features, the total particle
1103 numbers were enhanced to $208,700 \times 3$ (E_{A1}), $240,475 \times 3$ (E_{A2}), $260,021 \times 3$ (E_B) and $129,492$
1104 $\times 3$ (E_{D2}). The free energy landscapes were computed with 80, 80, 80 and 40 masked volumes
1105 bootstrapped by upper resolution limitations of 15, 15, 15 and 20 Å, respectively. Several 3D
1106 classes with the particle numbers of 192,219, 2,539, 3,982 and 609 were obtained by the particle-
1107 voting procedure on the zoomed-in free energy landscape of state E_{A1}, while the case of state E_{A2}
1108 gave four classes containing 147,108, 5,842, 5,500 and 33,083 particles (Extended Data Fig. 6e,
1109 f). Likewise, the particle numbers of 3D classes on the zoomed-in free energy landscape of state
1110 E_B were 173,931, 5,117 and 9,754 (Extended Data Fig. 6g); and the zoomed-in free energy
1111 landscape of state E_{D2} resulted in four classes having 61,580, 6,192, 24,674 and 1,673 particles,
1112 respectively (Extended Data Fig. 6h).

1113 To detect and improve RPN1-bound ubiquitin densities, a local mask around RPN1 was used,
1114 with 15 Å resolution limit applied in the volume-bootstrapping step. The zoomed-in free energy
1115 landscape around state E_{A1} computed from 120 volumes resulted in five classes with the particle
1116 numbers of 128,161, 7,754, 6,557, 6,826 and 3,937. Five 3D classes on the zoomed-in free
1117 energy landscape of E_{A2} , also computed with 120 volumes, including 81,612, 27,483, 12,247,
1118 26,029 and 12,777 particles, were analyzed (Extended Data Fig. 6c, d). In the case of the
1119 ubiquitin-binding site on the α 5 subunit of the CP, five 3D classes with the particle numbers of
1120 136,071, 19,351, 4,100, 131,570 and 4,932 were generated by particle voting on the zoomed-in
1121 free energy landscape of E_D computed with 120 volumes, which were bootstrapped from 326,409
1122 $\times 3$ particles via the mask containing this ubiquitin-binding site and no high-resolution restriction
1123 (Extended Data Fig. 6i). During these analyses, all masked volume-bootstrapping steps were
1124 performed for 50 iterations, whereas unmasked 3D classifications were performed for 30
1125 iterations with the initial reference low-pass filtered to 60 Å. At the last step, 3D refinement and
1126 reconstruction of each class was done to finalize the high-resolution structure determination.

1127 To exploit intermediate conformations during the substrate translocation initiation, a zoomed-
1128 in free-energy landscape was computed for the focused 3D classification procedure. First, the
1129 free energy landscape of all $3,254,352 \times 3$ particles was computed and analyzed. Then the
1130 zoomed-in free energy landscape of the states E_C and E_D containing $2,521,686 \times 3$ particle
1131 images were computed from 1,000 volumes that were bootstrapped without masking or
1132 resolution restriction (Extended Data Fig. 6b). For further zoomed-in processes, the particles
1133 around the translocation initiation states (from E_C to E_{D0}) on this free energy landscape were
1134 extracted by the distance-based 3D classification strategy. Subsequently, these particles were
1135 augmented to the number of $410,098 \times 3$ to generate 160 volumes for the computation of the
1136 zoomed-in free energy landscape with the RP mask and no resolution restriction imposed in the
1137 volume bootstrapping, which led to the 3D classes E_{C1} , E_{C2} , and $E_{D0.1}$ with the particle number of
1138 68,506, 77,545, and 25,755, respectively (Extended Data Fig. 6j). Moreover, state $E_{D0.3}$ came
1139 from two clusters with 86,415 and 83,107 particles merged together on the unmasked free energy
1140 landscape, and the classes $E_{D0.2}$ and $E_{D1.1}$ including 105,081 and 51,808 particles, respectively,
1141 were also obtained after particle voting on this free energy landscape. In the local areas of the
1142 state E_{D1} on the energy landscape, two clusters with 80,841 and 94,273 particles were merged to
1143 reconstruct the high-resolution structure of state $E_{D1.2}$, while states $E_{D1.1}$ and $E_{D1.3}$ with 40,696

1144 and 145,506 particles, respectively, were separated out from the clusters on this unmasked free
1145 energy landscape. In these studies, the maximum number of iterations in the 3D classifications of
1146 volume bootstrapping was 30, with the initial reference low-pass filtered to 60 Å routinely.

1147 Beyond resolving significantly more conformers from the same dataset, AlphaCryo4D also
1148 allows us to push the envelope of the achievable resolution of dynamic components and key
1149 metastable states due to its advantage in keeping more particles without sacrificing
1150 conformational homogeneity. To improve the resolution of state E_{D2}, a rigorous particle voting
1151 procedure was performed in each cluster on the unmasked free energy landscape (Fig. 3b, c),
1152 which improved the overall quality of particle dataset while classifying significantly more
1153 particles to this E_{D2} conformational class. Next, we conducted a focused 3D classification by
1154 using AlphaCryo4D to calculate the zoomed-in free energy landscape of the entire E_{D2} dataset to
1155 detect any potential conformational changes within this class. Five clusters near the energy wells
1156 of state E_{D2}, whose particle numbers were 154,661, 243,799, 198,221, 179,257 and 106,047,
1157 were investigated by separate high-resolution 3D refinement and reconstruction. The resulting
1158 refined density maps at 3.0-3.5 Å were found to be all in an identical conformation as previously
1159 reported². These five clusters were then merged together to refine a final 3D density map of state
1160 E_{D2}. Thus, AlphaCryo4D allowed us to obtain a new E_{D2} dataset that appears to retain high
1161 conformational homogeneity while including three-fold more particles, which improves its 3D
1162 reconstruction from the previously published resolution at 3.2 Å to 2.5 Å, measured by gold-
1163 standard Fourier shell correlation (FSC) at 0.143-cutoff. By contrast, in our previous work², we
1164 had attempted to include more E_{D2}-compatible 3D classes from 3D maximum-likelihood
1165 classification in RELION, which resulted in lower resolution at 3.3 Å by doubling the E_{D2}
1166 dataset, indicating that including more particles by conventional methods gave rise to higher
1167 heterogeneity in the class presumably due to increased misclassification.

1168 **Analysis of doubly and singly capped proteasomes**

1169 Previous cryo-EM analyses of the proteasomal states were nearly all focused on the RP-CP
1170 subcomplex, by converting double-cap (DC) proteasome particles to pseudo single-cap (SC)
1171 proteasome, which was always mixed with true SC particle images, in order to improve the
1172 resolution with conventional methods^{2,14-16,47,48}. As a result, the cryo-EM density of the CP gate
1173 in the other side distal to the RP in the RP-CP subcomplex has been an average of closed and
1174 open states with unknown stoichiometry. This has made it impossible to appreciate the difference

1175 between the SC and DC proteasomes in the previous studies. To remove this ambiguity, we
1176 reconstructed 8 density maps of the true SC proteasome and 36 density maps of the true DC
1177 proteasome including all possible combination of the 8 major RP-CP states. To reconstruct the
1178 density maps of the DC proteasome, pseudo-SC particles corresponding to 8 different RP states
1179 were voted out from the free energy landscape, with the sub-states belonging to the same RP
1180 state combined together. Then the particles with one RP-CP were extracted from the particle
1181 stacks to refine the RP and CP density maps with RP and CP contour masks applied in the local
1182 search step in RELION, respectively. For each reconstruction of the DC proteasome, two RP
1183 density maps on the opposite sides of the CP were expanded from $600 \times 600 \times 600$ pixels to 800
1184 $\times 800 \times 800$ pixels using RELION and aligned by the density of CP in Chimera before being
1185 merged together.

1186 Counting the particle number of the 36 states of the DC proteasome, we could derive the
1187 distribution of the DC states, p_{ij} , and that of RP p_i only, where i and j denote the states of two
1188 RPs in the same DC proteasome. Based on the value of p_{ij} and total particle number, the
1189 experimental state distribution of the DC proteasome was plotted for quantitative analysis in two
1190 dimensions with respect to the states of two RPs in the same DC proteasome (Fig. 3e). If the
1191 states of two RPs of the same DC proteasome were independent of each other, the predicted state
1192 distribution \tilde{p}_{ij} of the DC proteasome can be calculated as:

$$\tilde{p}_{ij} = p_i \cdot p_j$$

1193 By using the total particle number and experimentally measured p_i , the 2D state distribution of
1194 the DC proteasome with two uncoupled RPs was calculated for further comparison to investigate
1195 the conformational entanglement effect of the two RP states (Fig. 3f-h).

1197 **Atomic model building and refinement**

1198 To build the initial atomic model of the newly discovered states, we use previously published
1199 proteasome structures as a starting model and then manually improved in Coot⁴⁹. For the
1200 conformational states at resolutions lower than 5 Å, pseudo-atomic modelling was conducted in
1201 the following steps. First, each subunit was fitted as a rigid body, often in UCSF Chimera⁵⁰ as
1202 well as in Coot⁴⁹. Then, the local structural domains and secondary structure elements were fitted
1203 as a rigid body, with linking loops flexibly fitted and modelled. After the mainchain structures
1204 were well fitted, no further fitting of the sidechain rotamers were pursued due to insufficient
1205 resolution except for energy minimization to remove unrealistic side-chain clashes. For the

1206 conformational states at resolutions higher than 5 Å, the mainchain traces were first fit in Coot.
1207 Then, extensive fitting, adjustment and optimization of sidechain rotamers were conducted
1208 through local real-space refinement and manual rectification in Coot to the degree commensurate
1209 to the map resolution and quality. Atomic model refinement was conducted in Phenix⁵¹ with its
1210 real-space refinement program. We used both simulated annealing and global minimization with
1211 NCS, rotamer and Ramachandran constraints. Partial rebuilding, model correction and density-
1212 fitting improvement in Coot⁴⁹ were iterated after each round of atomic model refinement in
1213 Phenix⁵¹. The improved atomic models were then refined again in Phenix, followed by
1214 rebuilding in Coot⁴⁹. The refinement and rebuilding cycle were often repeated for three rounds or
1215 until the model quality reached expectation (Extended Data Table 2). All figures of structures
1216 were plotted in Chimera⁵⁰, PyMOL⁵², or ChimeraX⁵³. Local resolutions of cryo-EM density
1217 maps were evaluated using ResMap⁵⁴ or Bsoft Blocres program⁵⁵. Structural alignment and
1218 comparison were performed in both PyMOL and Chimera. Electrostatic surfaces were calculated
1219 by APBS plugin⁵⁶ in PyMOL.

1220 Given a large range of variations of local resolution in an expanded number of proteasome
1221 states and substates, as well as reconstructions with different stoichiometric ratio of RP versus
1222 CP, additional caveats and cautions were practiced in order to avoid misinterpretation and
1223 overall-fitting of atomic and pseudo-atomic models. First, when fitting the ubiquitin structure to
1224 the low-resolution local density, we consider both the existing homologous structural models as a
1225 modelling reference. Specifically, the fitting of diubiquitin to the density on RPN2 in states E_{A2.1},
1226 E_{A2.2}, and E_{B.2}, we took the NMR structure of the yeast di-ubiquitin-bound Rpn1 T1 site as a
1227 reference, because of the high structural homology between RPN1 and RPN2. For the fitting of
1228 RPN10-bound density, we also took into account the electrostatic complementarity (Extended
1229 Data Fig. 10). Second, even within an overall high-resolution cryo-EM map, it often presents
1230 certain local densities at a lower local resolution due to poor occupancy of ligands or flexibility
1231 of less well-folded segments. For example, for the nucleotide in RPT5 in states E_{D0.1} to E_{D1.3}, the
1232 high-resolution atomic model of ADP refined from other states like E_{C1} were used to fit these
1233 lower-local-resolution densities as a rigid body. However, the B-factors of the fitting atoms of
1234 ADP in RPT5 were reported to be more than twice higher than those of other nucleotides,
1235 indicating its partial occupancy or unstable binding. Thus, ADP fitting in RPT5 should be
1236 regarded tentative for the most or for the purpose of evaluation of nucleotide states rather than a

1237 reliable high-resolution atomic modeling. Similarly, the atomic models of these locally low-
1238 resolution features were only further adjusted with strict stereochemical constraints when the
1239 map resolution and features permit. Third, for the CP gate at the other side opposite to the RP in
1240 the RP-CP subcomplex reconstructed from a mixture of true and pseudo-SC proteasomes
1241 (converted from the DC proteasomes), their local densities in states $E_{D0.1}$ to E_{D2} appears to be an
1242 average of the open and closed states, and thus are weaker in amplitude than the rest of the CP.
1243 In the atomic model building of these reconstructions, we chose to model them with the closed
1244 CP gate state as long as their density resolution allows atomic modeling. This issue was
1245 completely solved when we separated the 3D classes of the SC and DC proteasomes and
1246 reconstructed their states respectively, where the atomic modelling of any CP gate no longer
1247 suffers from such ambiguities.

1248 **Quantum mechanical calculation**

1249 First-principles calculations on the electronic structures of the substrate-proteolytic site complex
1250 were conducted as described. In brevity, local coordinates of the substrate-bound CP near the
1251 catalytic site at residue Thr1 were taken out from the experimentally fitted atomic models of CP
1252 and the substrate, in both E_A and E_{D2} conformations. The proteolytic site is the Thr1 residue at
1253 the $\beta 2$ subunit but extended along the chain for another two residues to make the system less
1254 finite. Hydrogen atoms are added to complete the residues, and to saturate the system
1255 boundaries. The structural relaxations and electronic structure calculation were carried out using
1256 the density functional theory (DFT) method with norm-conserving pseudopotentials as
1257 implemented in the SIESTA code⁵⁷. To set up the initial conditions of the finite system, the
1258 hydrogen atom in the hydroxy group of Thr1 is manually relocated to the nearby nitrogen atom
1259 in the same residue, corresponding to the initial proton transfer in the catalytic mechanism. All
1260 hydrogen atoms were subsequently optimized without symmetric restrictions using the conjugate
1261 gradient algorithm and a 0.04 eV/Å maximum force convergence criterion while keeping the rest
1262 of the system fixed. The generalized gradient approximation (GGA) exchange-correlation
1263 density functional PBE³¹ was employed together with a double-zeta plus polarization basis set,
1264 and a mesh cutoff of 200 Ry (corresponds to 0.23 Å smallest grid size). The charge density and
1265 charge density difference contour maps were plotted with the Siesta Utility programs denchar
1266 and Python, respectively.

1267 **Data availability**

1268 The three-dimensional cryo-EM density maps of all new states are deposited into the Electron
1269 Microscopy Data Bank (EMDB) (www.emdatasource.org) under accession numbers to be
1270 provided upon formal publication of this manuscript). The coordinates are deposited in the
1271 Protein Data Bank (PDB) (www.wwpdb.org) (with accession numbers to be provided upon
1272 formal publication of this manuscript). Raw data are deposited into the Electron Microscopy
1273 Pilot Image Archive (www.ebi.ac.uk/pdbe/emdb/empiar) (with accession numbers to be provided
1274 upon formal publication of this manuscript). Source code of AlphaCryo4D is freely available for
1275 download (<http://ipccsb.dfci.harvard.edu/alphacryo4d/>).

1276

1277 **Acknowledgments.** The authors thank Q. Ouyang, A. Goldberg, D. Finley, S. Elsasser, M.
1278 Kirschner, Y. Lu, and for constructive discussions. This work was funded in part by the Natural
1279 Science Foundation of Beijing Municipality (grant No. Z18J008/Z180016), the National Natural
1280 Science Foundation of China (grant No. 11774012) and a gift academic grant from Intel
1281 Corporation. The cryo-EM data were collected at the Cryo-EM Core Facility Platform and
1282 Laboratory of Electron Microscopy at Peking University. The data processing was performed in
1283 the High-Performance Computing Platform at Peking University.

1284

1285 **Author contributions.** Y.M. and Z.W. conceived this study, devised the methodology and wrote
1286 the paper. Z.W. developed the deep learning system and conducted numerical studies of the
1287 system using the synthetic datasets. Z.W. and S.Z analyzed the experimental cryo-EM datasets
1288 and refined the density maps. W.L.W. conducted the quantum mechanical simulation. Y.M.
1289 supervised this study, verified the density maps, built and refined the atomic models, interpreted
1290 the data and drafted the manuscript with inputs from all authors.

1291

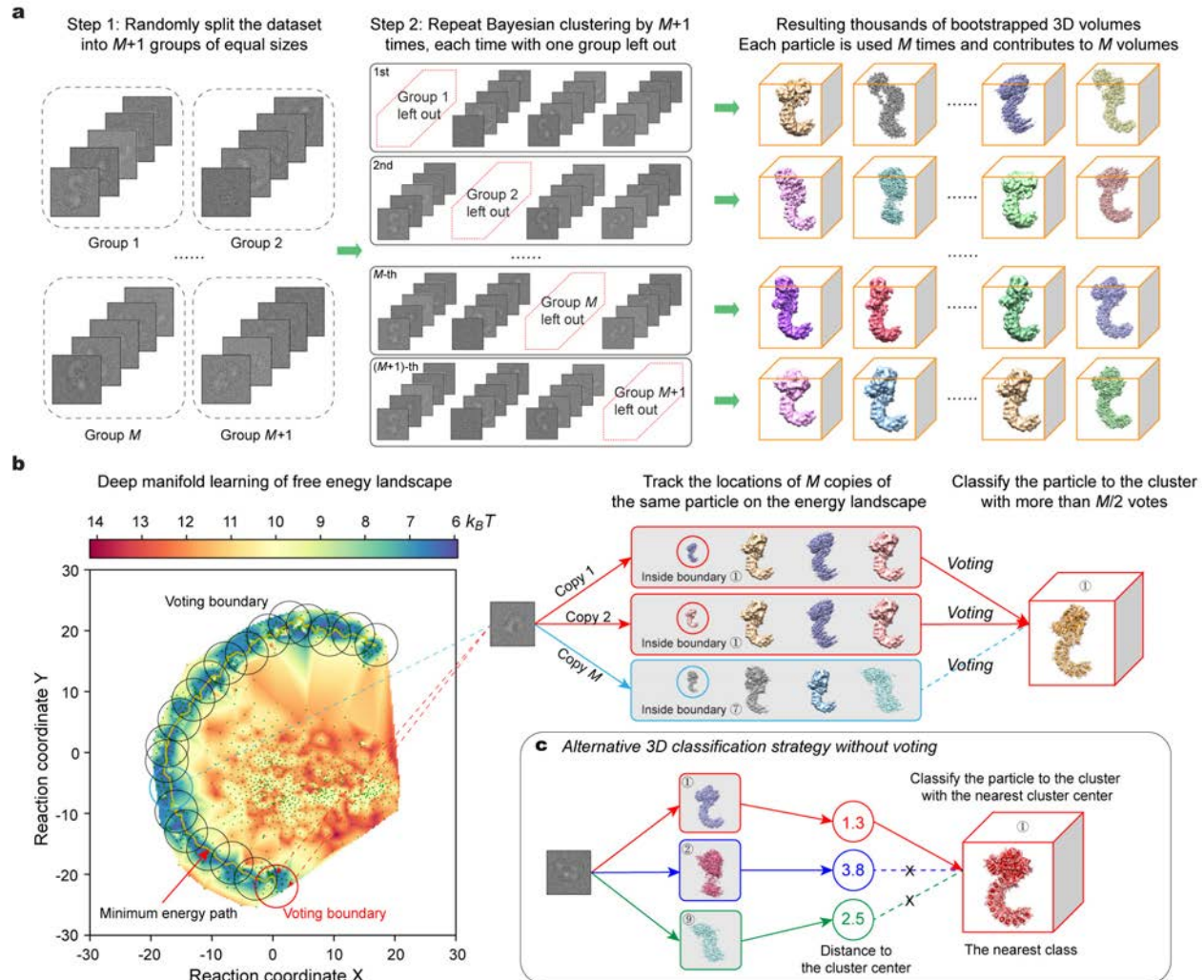
1292 **Competing interests.** The authors declare no competing financial interests.

1293

1294 **Correspondence and requests for materials** should be addressed to Y.M.

1295

1296

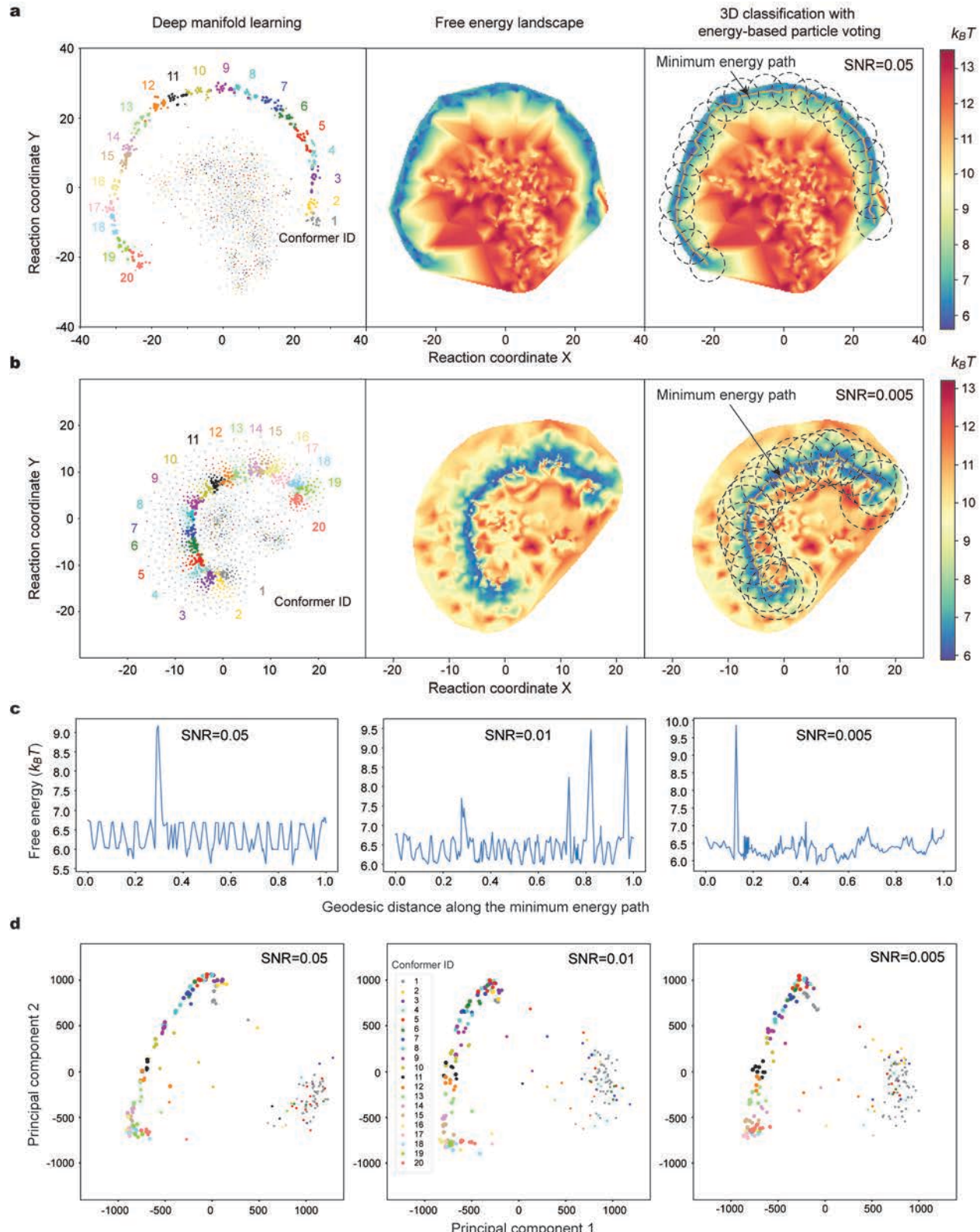


1297

1298 **Extended Data Fig. 1. Detailed algorithmic design of particle shuffling and voting in**
 1299 **AlphaCryo4D. a**, Schematic showing the method of particle shuffling for data augmentation and
 1300 bootstrapping of 3D volumes. In the step 1, all particles are split randomly into $M + 1$ groups
 1301 equally. Then the step 2 carries out the Bayesian clustering for reconstructions of 3D density
 1302 maps within each of the $M + 1$ particle sets that are shuffled via the leave-one-group-out
 1303 approach. After these two steps, thousands of 3D volumes are generated for the subsequent 3D
 1304 deep learning, with each particle contributing to M volumes. **b**, Schematic showing the
 1305 algorithmic concept of energy-based particle voting for 3D classification. The left panel shows
 1306 the free energy landscape obtained by deep manifold learning. After clustering along the
 1307 minimum energy path, all M locations of each particle on the free energy landscape can be
 1308 tracked to cast M votes. A vote of the particle is only counted for the cluster when it is mapped
 1309 within the voting boundary of the cluster, as indicated by the circles marked on the free-energy

1310 landscape. Eventually, this particle is classified to the 3D cluster with over $M/2$ votes from this
1311 particle. **c**, Alternative distance-based 3D classification method as a control in the analysis of
1312 algorithmic performance of particle voting. Instead of particle voting, each particle is directly
1313 classified to the cluster with the nearest clustering center among the M volume data points in the
1314 distance-based 3D classification strategy.

1315



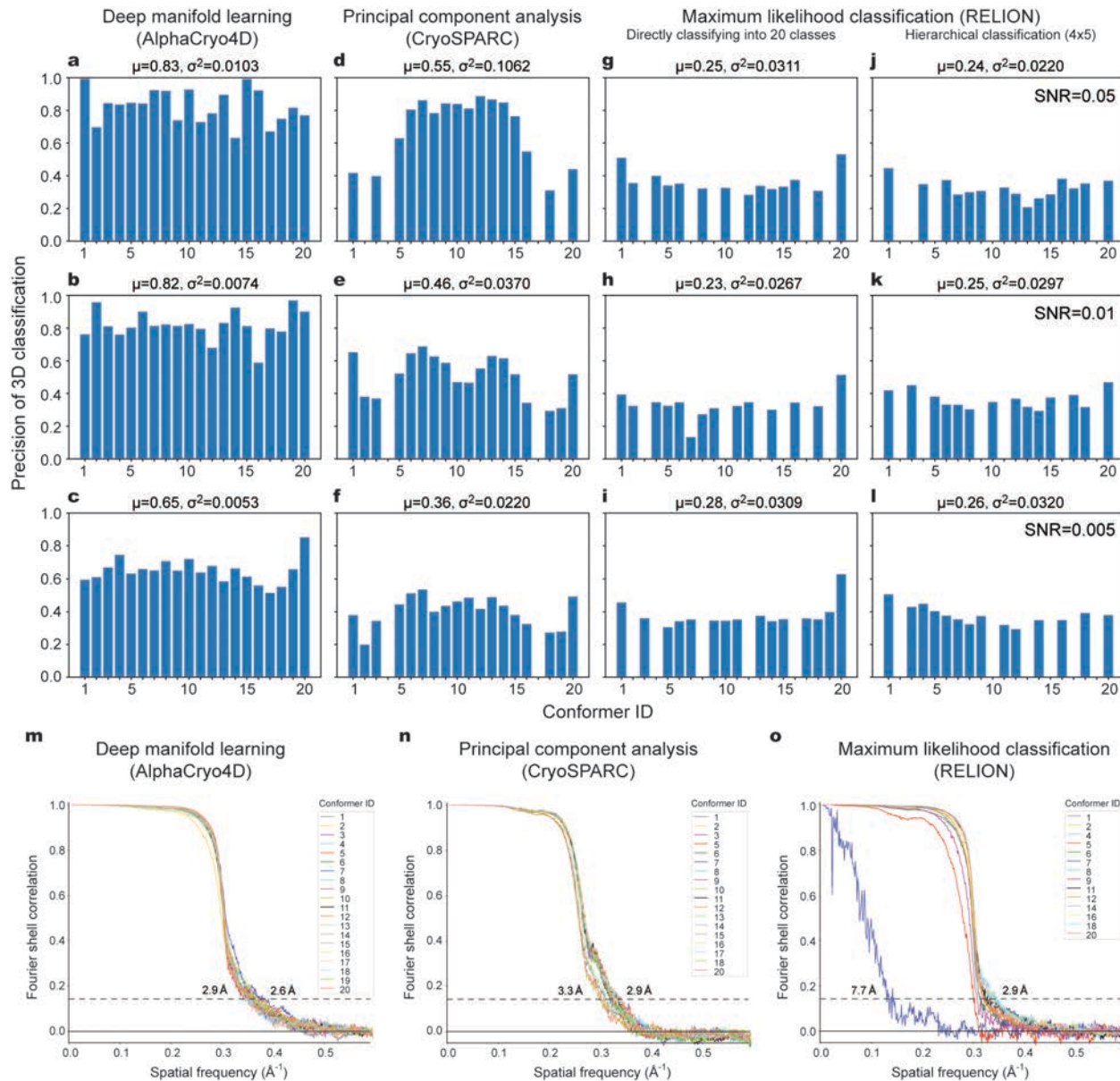
1316

1317 **Extended Data Fig. 2. Blind assessments of AlphaCryo4D and its comparison with the 3D**
 1318 **PCA method using the simulated heterogeneous NLRP3 datasets of different SNRs. a and**

1319 **b**, Reconstruction of the free energy landscape of the simulated NLRP3 datasets at SNRs of 0.05
1320 (**a**) and 0.005 (**b**) by the t-SNE algorithm using the bootstrapped volumes and their
1321 corresponding feature maps. Colors in the left panels indicate the ground truth of 3D volume data
1322 points. **c**, Free energy profiles along the MEP calculated by the string method in the 2D energy
1323 landscapes of the simulated NLRP3 datasets at SNRs of 0.05 (left), 0.01 (middle) and 0.005
1324 (right). **d**, Dimensionality reduction and 3D classification of the simulated datasets at three
1325 distinct SNRs by the 3D PCA method as the control of our algorithm evaluation. Colors of data
1326 points indicate the ground truth of their corresponding 3D volumes.

1327

1328



1329

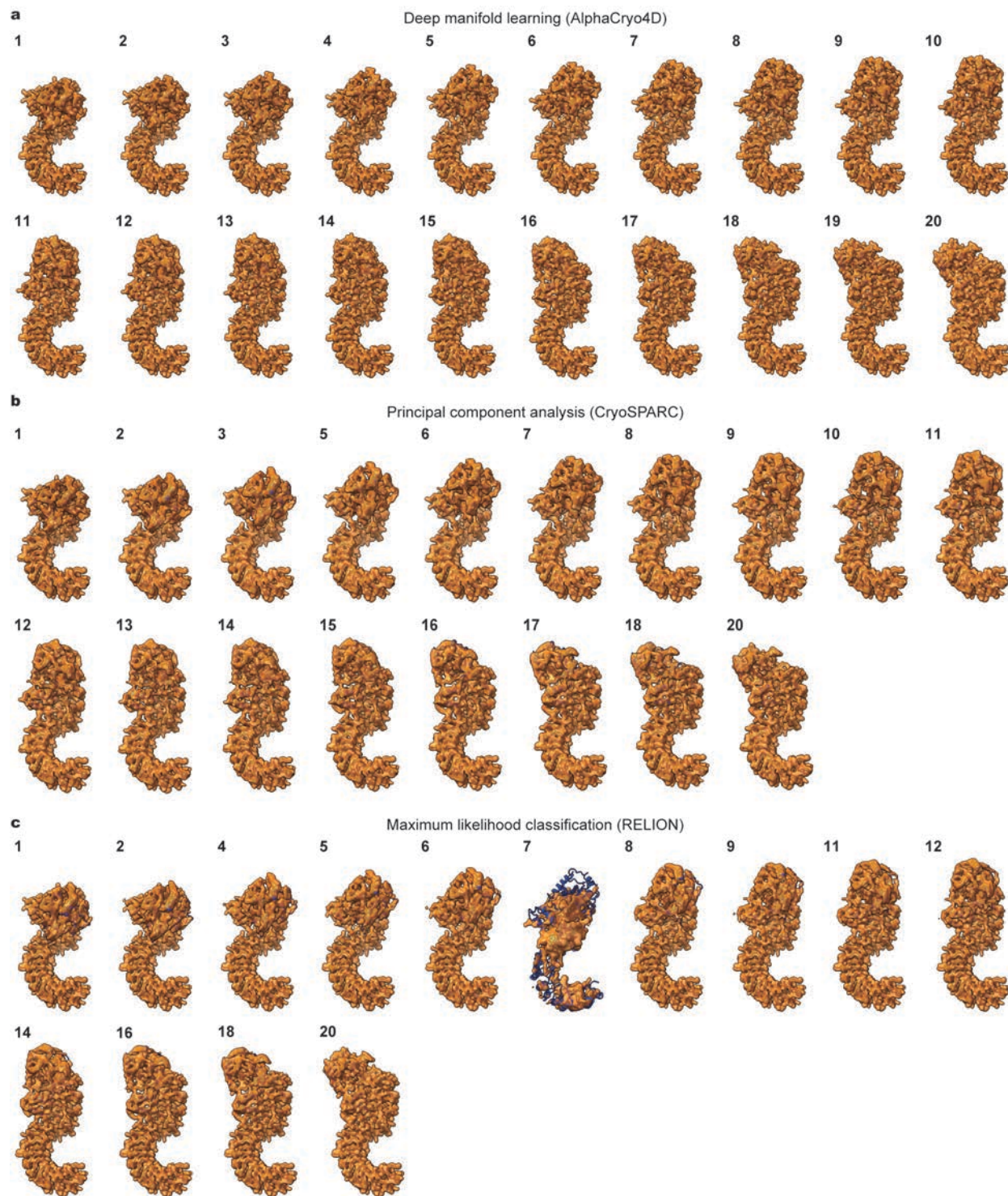
1330 **Extended Data Fig. 3. Performance comparison of AlphaCryo4D with existing methods**
 1331 **using the simulated heterogeneous NLRP3 datasets of different SNRs. a-l,** 3D classification
 1332 precision of the simulated datasets by AlphaCryo4D (**a-c**), PCA in CryoSPARC (**d-f**) and
 1333 maximum-likelihood classification in RELION (**g-l**). The results of SNRs of 0.05 (**a, d, g, j**),
 1334 0.01 (**b, e, h, k**) and 0.005 (**c, f, i, l**) are shown on three rows for side-by-side comparison. On the
 1335 top of each panel, the symbols of μ and σ^2 denote the mean and variance of precision,
 1336 respectively, with the values of missing classes treated as zeros. In the maximum-likelihood
 1337 classification of RELION, both direct and hierarchical strategies are compared in the study. **m-o**,
 1338 The gold-standard FSC of the 20 maps resulting from 3D classification by AlphaCryo4D (**m**), of

1339 the 18 maps resulting from the 3D classification by PCA in CryoSPARC (**n**), and of the 14 maps
1340 resulting from the maximum-likelihood 3D classification in RELION (**o**) on the simulated data
1341 of 0.01 SNR. They correspond to the precision results presented in panels (**b**), (**e**) and (**h**),
1342 respectively.

1343

1344

1345

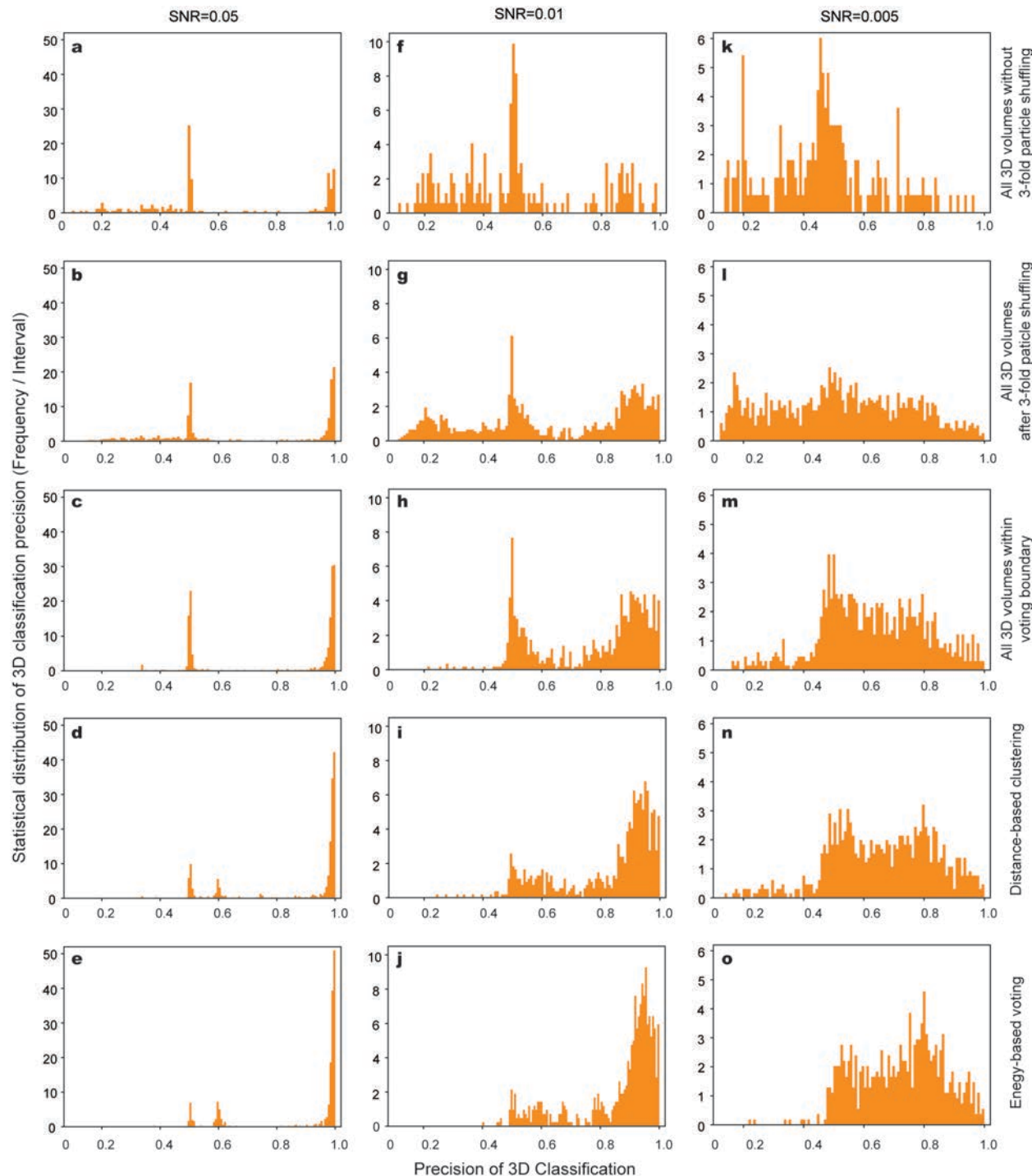


1347 **Extended Data Fig. 4. Map assessment of AlphaCryo4D in reconstructions of**
1348 **conformational continuum in comparison with conventional methods on the simulated data**
1349 **of 0.01 SNR. a,** The 20 maps of NLRP3 resulting from the 3D classification by AlphaCryo4D.
1350 **b,** The 18 maps of NLRP3 resulting from the 3D classification by PCA in CryoSPARC. **c,** The

1351 14 maps of NLRP3 resulting from the 3D classification by ML3D in RELION. All maps are
1352 shown in transparent surface representations superimposed with their corresponding atomic
1353 models of the ground truth in cartoon representations, which are fitted to the maps as rigid bodies
1354 without further atomic modelling. The conformer ID numbers are marked on the upper left of
1355 each map panel. The results shown in panels (a), (b) and (c) correspond to the FSC results shown
1356 in panels (m), (n) and (o) of Extended Data Fig. 3, respectively.

1357

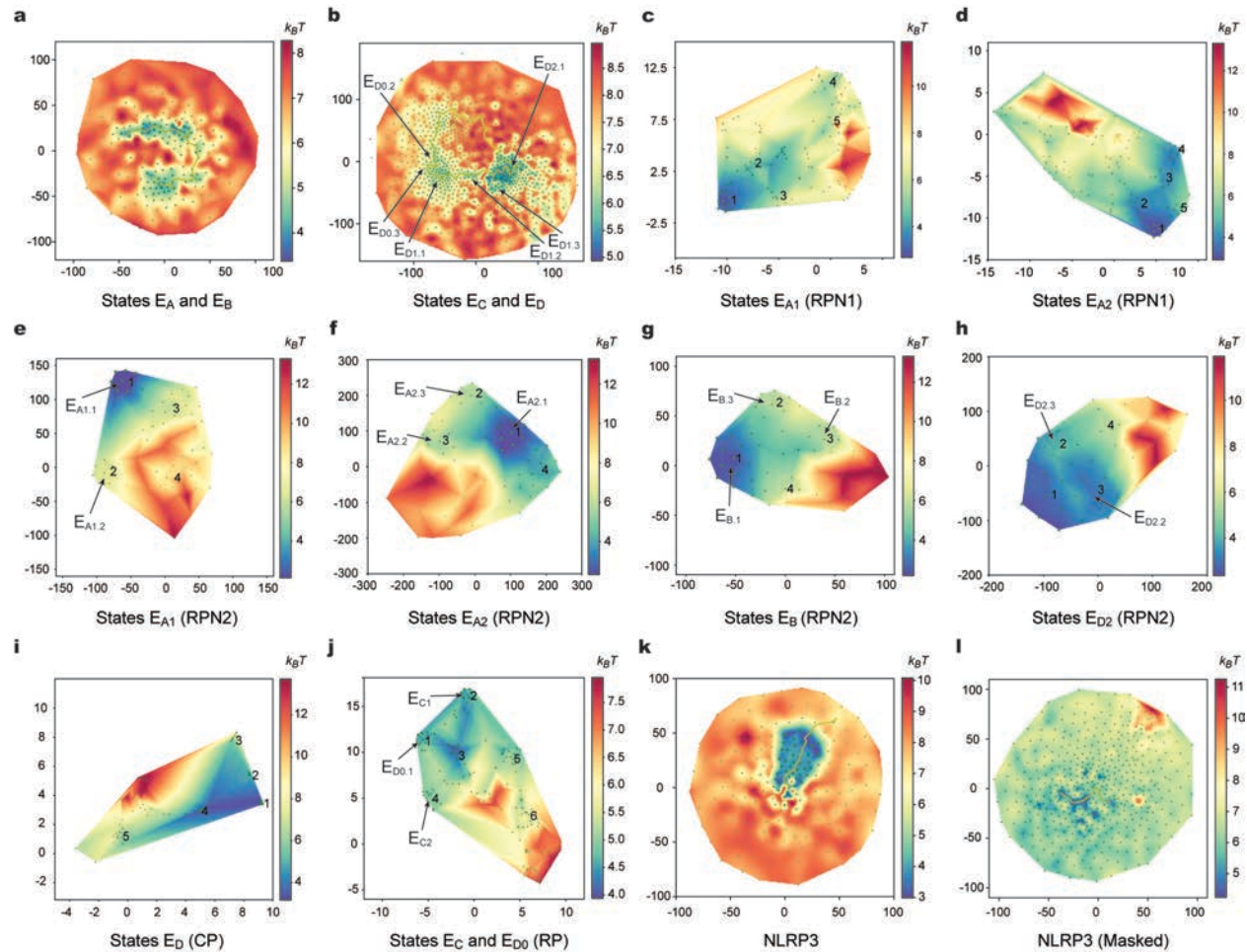
1358



1359

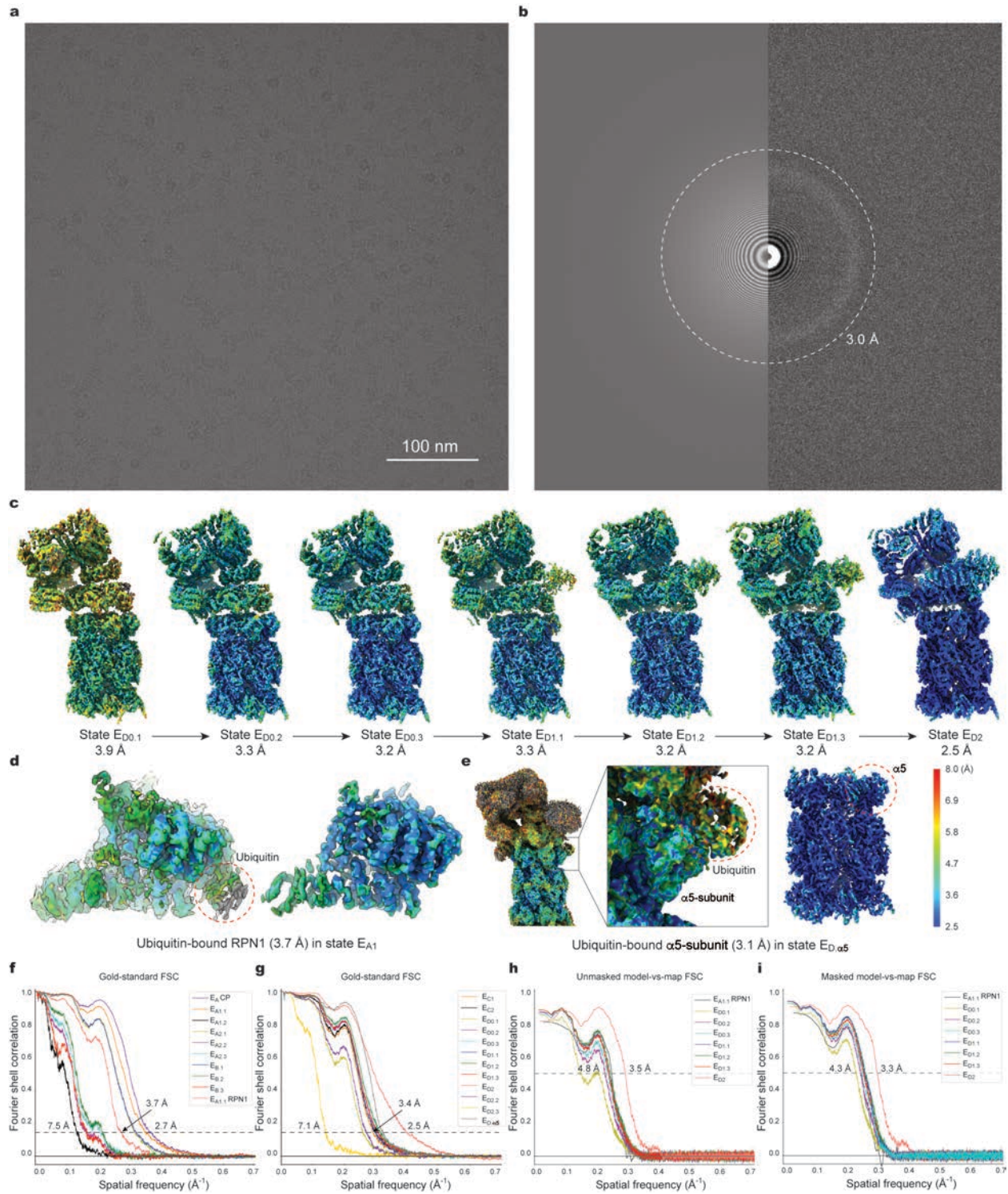
1360 **Extended Data Fig. 5. Mechanistic characterizations of the improvement of 3D**
1361 **classification precision in the intermediate steps of AlphaCryo4D using the simulated**
1362 **NLRP3 datasets of three typical SNRs. a-e,** Precision analysis on the simulated data of SNR of
1363 **0.05. f-j,** Precision analysis on the simulated data of SNR of 0.01. **k-o,** Precision analysis on the
1364 **simulated data of SNR of 0.005. a, f, k,** Statistical distribution of 3D classification precision in

1365 bootstrapped 3D volumes without particle shuffling. **b, g, l**, Distribution of 3D classification
1366 precision in bootstrapped 3D volumes after 3-fold particle shuffling. **c, h, m**, Distribution of
1367 classification precision in bootstrapped 3D volumes screened by voting boundary on the free
1368 energy landscape. **d, i, n**, Distribution of classification precision in bootstrapped 3D volumes
1369 after distance-based 3D clustering in the absence of particle voting as a control. **e, j, o**,
1370 Distribution of classification precision in bootstrapped 3D volumes after energy-based particle
1371 voting.
1372
1373
1374
1375
1376
1377
1378
1379
1380
1381



1382

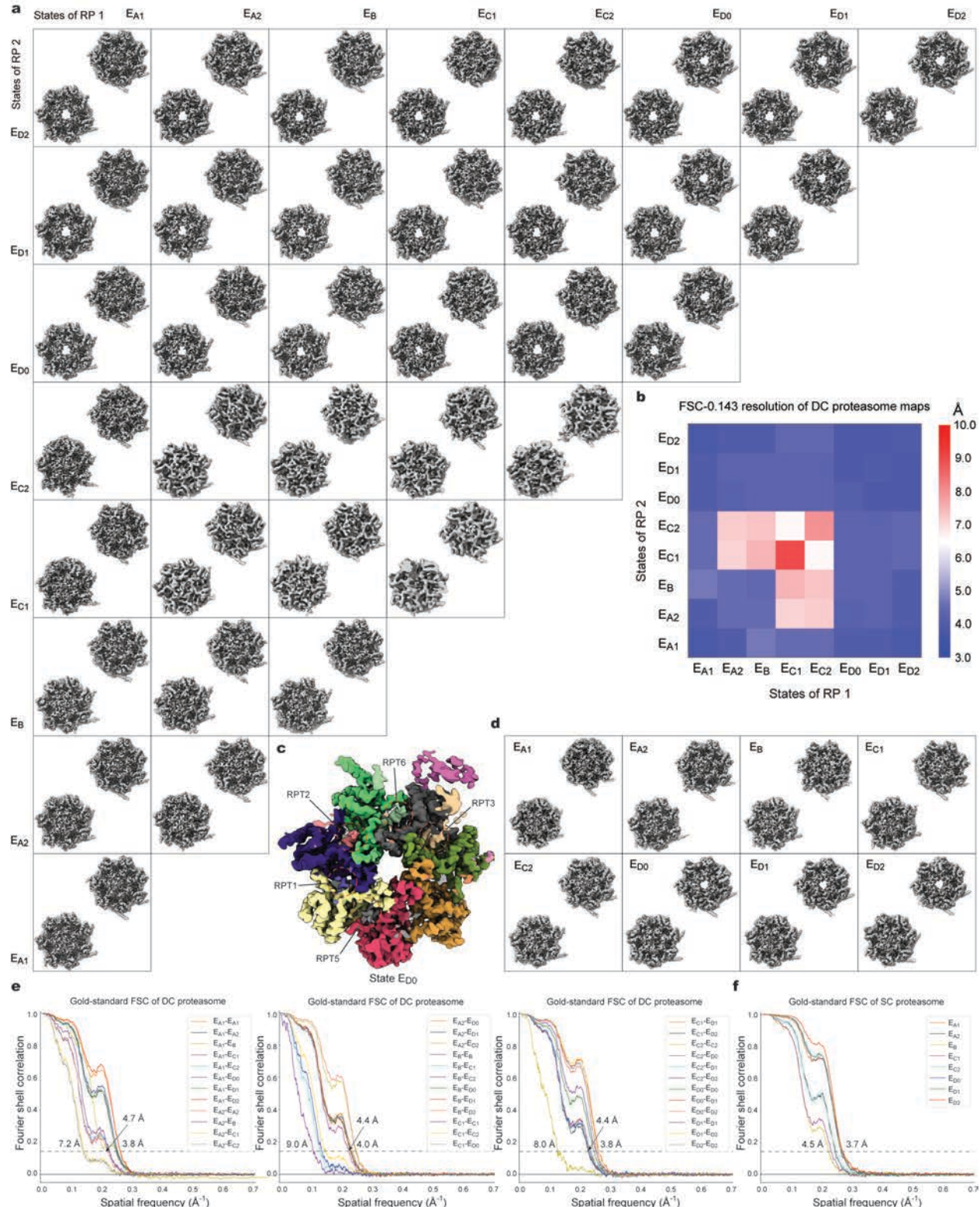
1383 **Extended Data Fig. 6. The zoomed-in free-energy landscape used for focused 3D**
 1384 **classifications of AlphaCryo4D on the experimental cryo-EM datasets for finding new**
 1385 **states of the substrate-bound proteasome. a-j,** The zoomed-in local energy landscapes of the
 1386 substrate-bound human proteasome by AlphaCryo4D are shown for state E_A and E_B in (a), for
 1387 states E_C and E_D in (b), for states E_{A1} and E_{A2} with 3D mask focusing on RPN1 in (c) and (d), for
 1388 states E_{A1} , E_{A2} , E_B and E_{D2} with 3D masking around RPN2 in (e), (f), (g) and (h), respectively,
 1389 for combined states of E_D with masking around CP (i), and for combined states of E_C ad E_{D0} with
 1390 3D mask focusing on the RP (j). **k and l,** The energy landscape computed from the experimental
 1391 cryo-EM dataset of the NLRP3-NEK7 complex without (k) and with a global contour mask (l).



1392

1393 **Extended Data Fig. 7. Cryo-EM reconstructions and resolution assessment of novel**
 1394 **proteasomal states determined by AlphaCryo4D. a,** A typical raw micrograph of the
 1395 substrate-bound human proteasome recorded under the super-resolution counting mode of Gatan
 1396 K2 Summit direct electron detector. **b,** The power spectrum of the micrograph shown in panel

1397 (a), with the 3 Å resolution ring marked by the dashed circle. c, Local resolution measurement of
1398 the seven sequential states corresponding to the open CP gate states E_{D0.1} to E_{D2}. d, The local
1399 resolution measurement of the density maps of ubiquitin-bound RPN2 structure in state E_{A1} at
1400 two different contour levels. e, The local resolution measurement of the CP in state E_{D.α5}, with a
1401 ubiquitin-moiety bound to the α5 subunit. The right panel shows the CP density map at higher
1402 contour level. The color bar for local resolutions is shown for all panels in c-e, which were all
1403 measured by ResMap⁵⁴. f and g, The gold-standard FSC plots of the 20 conformers of the RP-CP
1404 subcomplex. h and i, The FSC curves calculated between the experimental cryo-EM maps and
1405 their corresponding atomic models for newly discovered states or improved states without (h)
1406 and with (i) masking in the calculations.



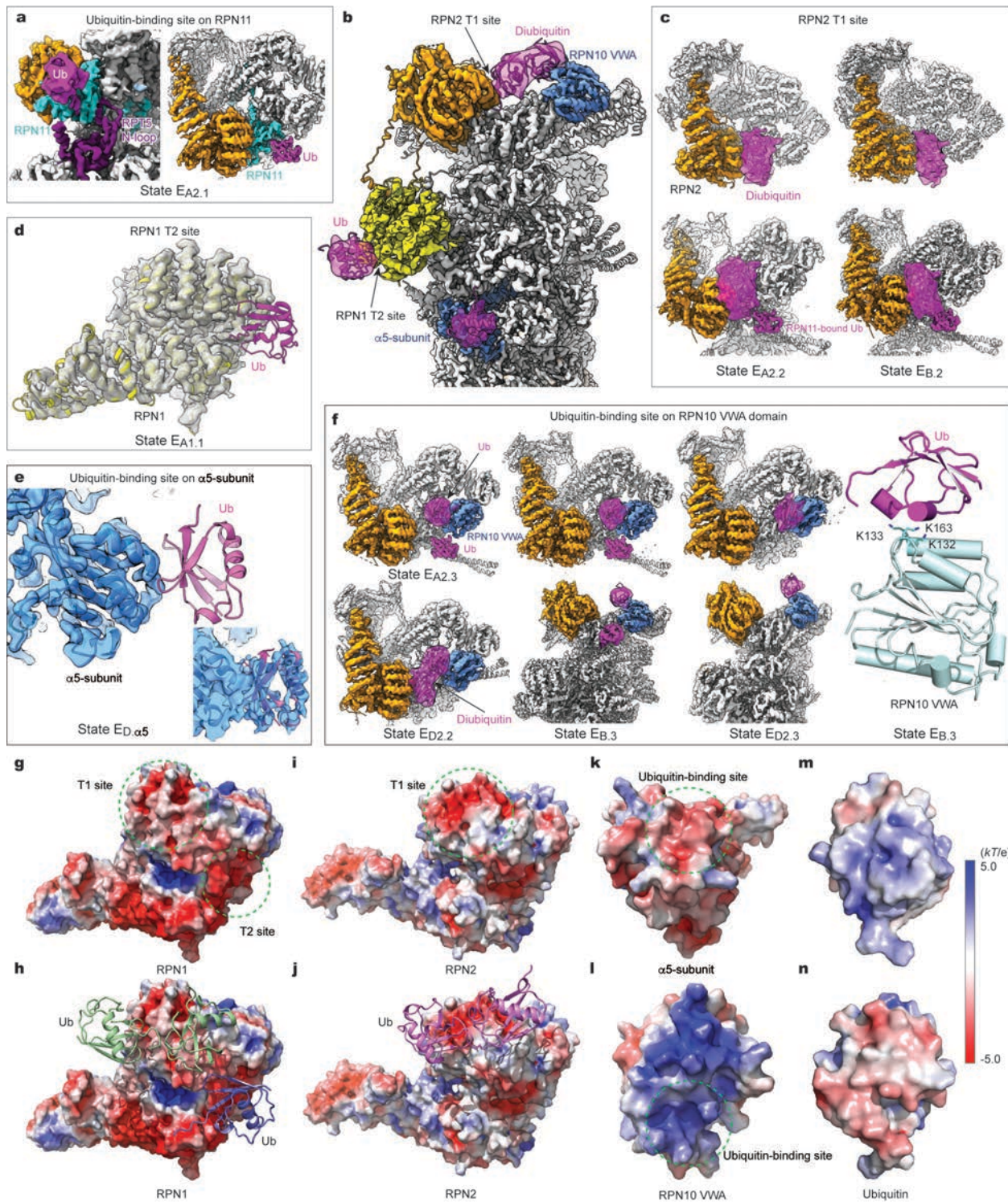
1407

1408 **Extended Data Fig. 8. Cryo-EM analysis of the doubly capped (DC) and singly capped (SC)**
1409 **proteasomes. a,** The CP gate states of the 36 density maps of distinct conformational states of
1410 the DC proteasome. All density maps shown are low-pass filtered to their measured resolutions

1411 by the gold-standard FSC-0.143 cutoff without amplitude correction of B-factors. **b**, The FSC-
1412 0.143 resolution matrix of the 36 DC proteasomal states. **c**, The RP-CP interface of state E_{D0},
1413 showing five C-terminal tails inserted into the inter-subunit surface pockets of α -ring. **d**, The CP
1414 gate states of the 8 density maps of distinct conformational states of the SC proteasome, with the
1415 upper right image in each panel corresponding to the RP-proximal side of the CP gate, and the
1416 lower left image to the RP-distal side of the CP gate. **e**, The gold-standard FSC plots of the 36
1417 conformers of the DC proteasome. **f**, The gold-standard FSC plots of the 8 conformers of the SC
1418 proteasome.



1420 **Extended Data Fig. 9. 44 cryo-EM reconstructions of the SC and DC proteasomes classified**
1421 **from the same experimental dataset by AlphaCryo4D. a,** The density maps of 8 distinct
1422 conformational states of the SC proteasome. **b,** The density maps of 36 distinct conformational
1423 states of the DC proteasome. All maps are filtered to their respective gold-standard FSC-0.143
1424 resolutions without amplitude correction of B-factors and are differentially colored by their
1425 subunits in ChimeraX⁵³.

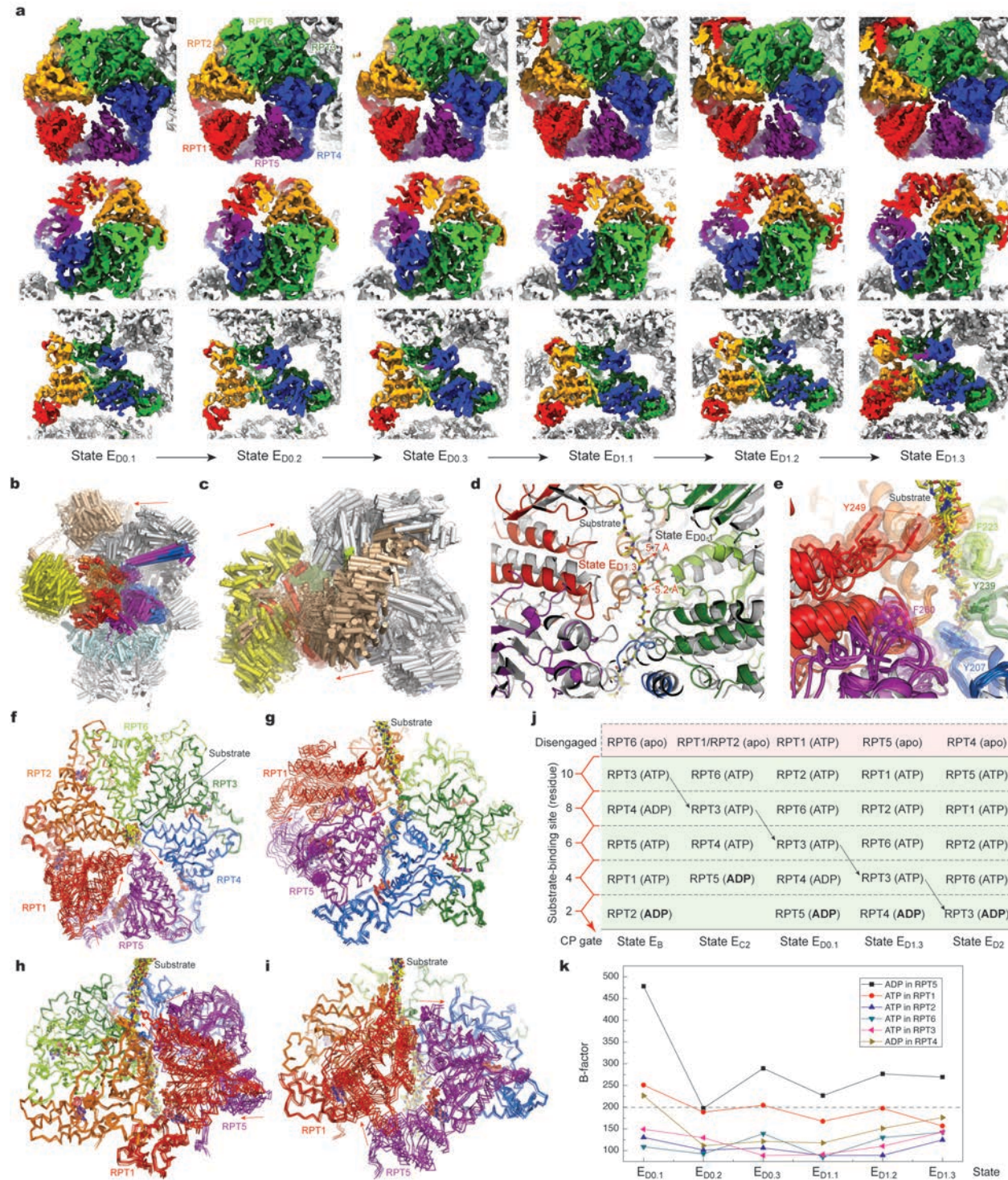


1426

1427

Extended Data Fig. 10. Structural analysis of ubiquitin-binding sites at high resolution. a,
1428 Cryo-EM density of state EA2.1 shows the improved resolution localized around RPN11-bound
1429 ubiquitin and the RPT5 N-loop as compared to previously determined state EA2. Ub, ubiquitin. **b,**
1430 High-resolution cryo-EM density of state ED2 superimposed with ubiquitin densities in state ED2.2

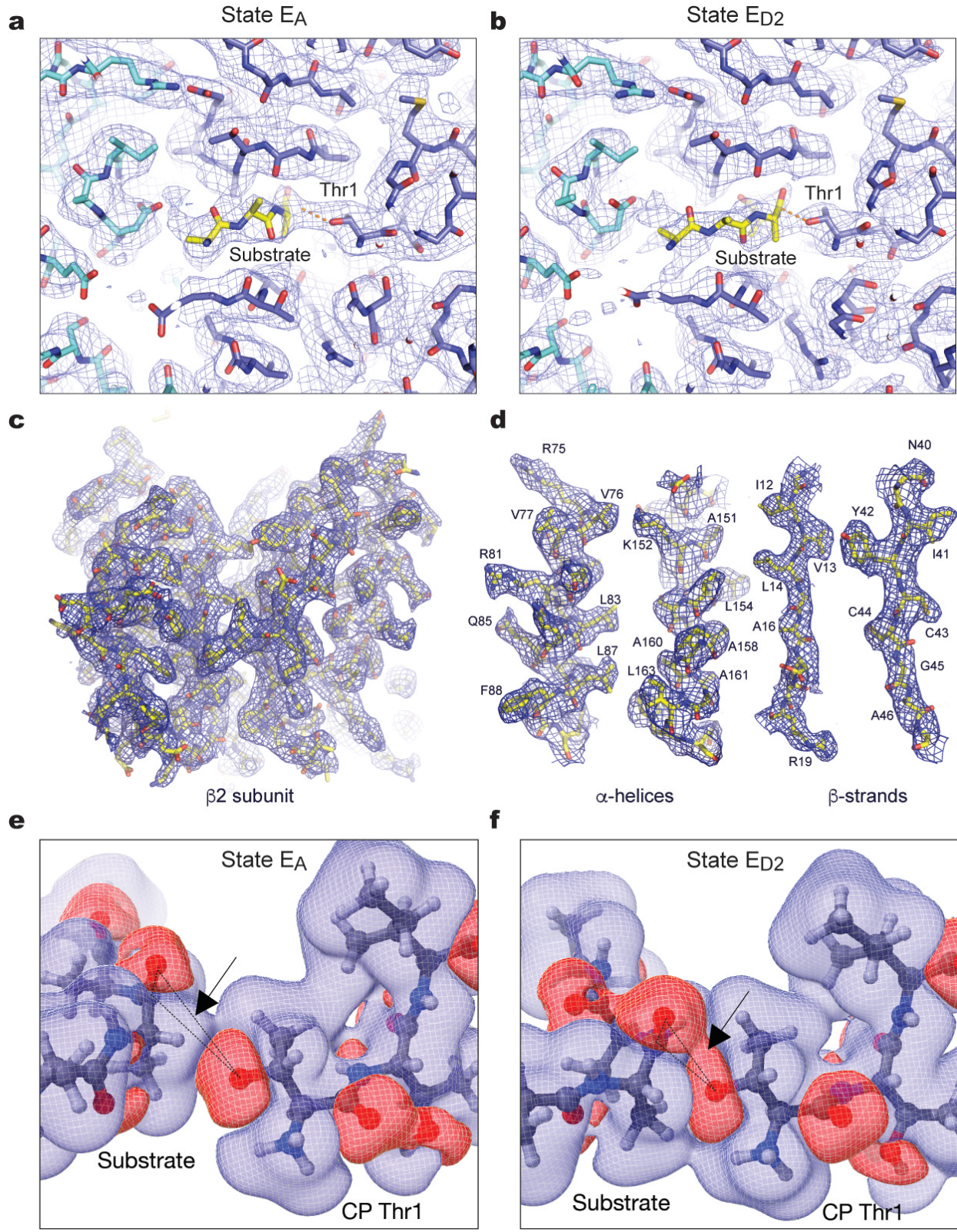
1431 highlighted as magenta, showing that a diubiquitin chain in contact with both the RPN2 T1 site
1432 and the RPN10 VWA domain. The atomic model of state E_{D2.2} in cartoon representation is
1433 superimposed with the density map. **c**, Closeup view of the RPN2-bound diubiquitin density in
1434 states E_{A2.2} (left column) and E_{B.2} (right column) in two different perspectives, with the lower
1435 row showing the coexistence of the RPN11-bound ubiquitin and the RPN2-bound diubiquitin. **d**,
1436 The refined 3.7-Å RPN1 density map from state E_{A1.1} in transparent surface representation
1437 superimposed with its atomic model with ubiquitin bound to the RPN1 T2 site. **e**, Closeup view
1438 of the α 5-subunit bound with ubiquitin in the refined 3.1-Å density map of state E_{D. α 5}. The cryo-
1439 EM density of the α 5-subunit is shown in transparent surface representation superimposed with
1440 its atomic model. Inset shows the ubiquitin density in transparent surface representation
1441 superimposed with its atomic model. **f**, Closeup views of the RPN10-bound ubiquitin densities in
1442 states E_{A2.3}, E_{B.3}, and E_{D2.3}. Right panel shows the pseudo-atomic model of ubiquitin interaction
1443 with the RPN10 VWA domain. **g-l**, The electrostatic surfaces of RPN1, RPN2, RPN10 and α 5-
1444 subunit show the charge complementarity of the RPN1 T1 and T2 (panels **g**, **h**), RPN2 T1
1445 (panels **i**, **j**) and α 5-binding (panel **k**) sites of ubiquitin are all acidic. By contrast, the RPN10
1446 VWA site is basic (panel **l**), suggesting that it may bind the acidic side of the ubiquitin molecule.
1447 **m** and **n**, The electrostatic surface of the ubiquitin shows one side that is basic (panel **m**) and the
1448 other side acidic (panel **n**).



1449

1450 **Extended Data Fig. 11. Cryo-EM structures of six sequential intermediate states between**
 1451 **E_C2 and $E_{D1.3}$.** **a**, Cryo-EM density maps of the AAA-ATPase motor in six sequential states from
 1452 $E_{D0.1}$ to $E_{D1.3}$ from three different viewing angles. The substrate densities are highlighted in
 1453 yellow. **b**, Superposition of the seven structures in cartoon representations from a lateral

1454 perspective, with all structures aligned together based on their CP structures, showing the RP
1455 movements relative to the CP. **c**, Superposition of the six structures in cartoon representations
1456 from a top-view perspective, with all structures aligned together based on their CP structures. **d**,
1457 Measurement of substrate movement between states $E_{D0.1}$ and $E_{D1.3}$ relative to the CP, suggesting
1458 that the substrate is translated ~5-6 Å during the process of ADP release in RPT5 and of RPT1
1459 re-association with the substrate. **e**, The closeup view of the pore-1 loop interaction with the
1460 substrate with all six states superimposed after aligned together based on the structures of RPT3,
1461 RPT4 and RPT6. **f-i**, Superposition of the six sequential states with their RPT3, RPT4 and RPT6
1462 aligned together. Red arrows show the direction of subunit movements in RPT1 and RPT5. **j**, A
1463 diagram illustrating the axial stepping of the substrate-interacting pore-1 loops that is coupled
1464 with ATP hydrolysis in the RPT subunits, revised from the previously published results based on
1465 the present study². **k**, The average B-factor of the nucleotides in six ATPase subunits fitted to the
1466 cryo-EM densities of states $E_{D0.1}$ to $E_{D1.3}$ and computed by Phenix in real-space refinement
procedure⁵¹. The high B-factor of ADP fitted in RPT5 indicates its low occupancy or unstable
1467 association and suggests that the ADP in RPT5 undergoes dissociation in this process.
1468



1472 subunit superimposed with the cryo-EM density map of state E_A at 2.7 Å. **b**, The atomic model
1473 of substrate-bound catalytic active site of the β2-subunit superimposed with the cryo-EM density
1474 map of state E_{D2} at 2.5 Å. **c**, Closeup view of the cryo-EM density of the β2-subunit in state E_{D2}
1475 shown in blue mesh representation superimposed with the atomic model. **d**, Cryo-EM densities
1476 of the typical secondary structure elements in the β2-subunit of state E_{D2} shown as blue mesh
1477 representation superimposed with their corresponding atomic models. The residues are labelled.
1478 The densities are shown at 4σ level and exhibit structural features consistent with 2.5-Å
1479 resolution. **e** and **f**, 3D Charge density difference map showing the interactions between the
1480 substrate polypeptide and the residue Thr1 in the β2-subunit of the CP. The red color labels an
1481 iso-surface of charge increase while the blue color labels charge decrease, both at a level of 0.04
1482 e/Å². The charge increase region at the Thr1-Oγ atom is elongated sideways, and the substrate
1483 position in the E_{D2} state provides both a proximity and orientation alignment for the pair to
1484 interact. The dashed line triangle shows the plane in which the detailed charge difference
1485 contours are plotted as shown in Fig. 6c, d.

1486

1487

1488 **Extended Data Table 1. Hyperparameters of the deep residual networks in the 3D**
1489 **autoencoder.** Optimizer: Adam. Epochs: 50. Initial learning rate: 0.01. A factor of 0.1 and
1490 patience of 3 means that the learning rate will times 0.1 (factor) if the loss function does not
1491 improve in 3 (patience) epochs. Batch size: 32 (for the three simulated datasets), 8 (for the
1492 substrate-bound proteasome dataset).

Layer name	Output size (simulation)	Output size (proteasome)	Network structure
Conv1	200 × 200 × 200	300 × 300 × 300	5 × 5 × 5, 2
Conv2_x	100 × 100 × 100	150 × 150 × 150	3 × 3 × 3, 2, stride 2
Conv3_x			3 × 3 × 3, 2
Conv4_x	50 × 50 × 50	75 × 75 × 75	3 × 3 × 3, 1, stride 2
Conv5_x			3 × 3 × 3, 1
Conv6_x (encoding)	100 × 100 × 100	150 × 150 × 150	3 × 3 × 3, 1
TransConv7_x			3 × 3 × 3, 1, stride 2
TransConv8_x	200 × 200 × 200	300 × 300 × 300	3 × 3 × 3, 1
TransConv9_x			3 × 3 × 3, 2, stride 2
TransConv10_x			3 × 3 × 3, 2
TransConv11			5 × 5 × 5, 1

1493

1494

1495 **Extended Data Table 2. Cryo-EM data collection, refinement and validation statistics**

	E _A	E _{A1.1}	E _{A1.2}	E _{A2.1}	E _{A2.2}	E _{A2.3}	E _{B.1}	E _{B.2}
Data collection and processing								
Magnification								
Magnification	105,000	105,000	105,000	105,000	105,000	105,000	105,000	105,000
Voltage (kV)	300	300	300	300	300	300	300	300
Electron exposure (e-/Å ²)	44	44	44	44	44	44	44	44
Defocus range (μm)	-0.6 to -3.5	-0.6 to -3.5	-0.6 to -3.5	-0.6 to -3.5	-0.6 to -3.5	-0.6 to -3.5	-0.6 to -3.5	-0.6 to -3.5
Pixel size (Å)	0.685	0.685	0.685	0.685	0.685	0.685	0.685	0.685
Symmetry imposed	C1	C1	C1	C1	C1	C1	C1	C1
Initial particle images (no.)	3,254,352	3,254,352	3,254,352	3,254,352	3,254,352	3,254,352	3,254,352	3,254,352
Final particle images (no.)	339,327	192,219	2,539	147,108	5,500	5,842	173,931	9,754
Map resolution (Å)	2.7	2.9	7.5	3.2	6.0	4.8	3.1	4.7
FSC threshold	0.143	0.143	0.143	0.143	0.143	0.143	0.143	0.143
Map resolution range (Å)	2.5-8.0	2.5-8.0	7.0-20.0	2.5-8.0	5.5-20.0	3.0-8.0	2.5-8.0	4.5-20.0
Refinement								
Initial model used	6MSB	6MSB		6MSD			6MSE	
Model resolution (Å)	3.2	3.4		3.5			3.4	
FSC threshold	0.5	0.5		0.5			0.5	
Model resolution range (Å)	2.5-8.0	2.7-8.0		3.0-8.0			2.9-8.0	
Map sharpening <i>B</i> factor (Å ²)	-25	-28		-30			-30	
Model composition								
Non-hydrogen atoms	63654	104938	105088	105426	106630	106028	105147	106351
Protein residues	8203	13391	13543	13418	13570	13494	13400	13552
Ligands	11	12	12	12	12	12	9	9
<i>B</i> factors (Å ²)								
Protein	131.13	145.9	145.9	151.26			182.77	
Ligand	125.87	110.13	110.13	108.00			123.85	
R.m.s. deviations								
Bond lengths (Å)	0.008	0.007	0.007	0.006	0.006	0.006	0.006	0.006
Bond angles (°)	0.908	1.013	1.013	1.005	1.005	1.005	1.017	1.017
Validation								
MolProbity score	1.49	1.76	1.76	1.76	1.76	1.76	1.83	1.83
Clashscore	2.72	4.86	4.86	4.91	4.91	4.91	5.57	5.57
Poor rotamers (%)	0.47	0.54	0.54	0.5	0.5	0.5	0.46	0.46
Ramachandran plot								
Favored (%)	93.3	91.34	91.34	91.42	91.42	91.42	90.89	90.89
Allowed (%)	6.52	8.36	8.36	8.33	8.33	8.33	8.77	8.77
Disallowed (%)	0.18	0.3	0.3	0.25	0.25	0.25	0.34	0.34

1496

1497

1498

1499

1500

1501

1502 Cryo-EM data collection, refinement and validation statistics (continued)

	E _{B.3}	E _{C1}	E _{C2}	E _{D0.1}	E _{D0.2}	E _{D0.3}	E _{D1.1}	E _{D1.2}
Data collection and processing								
Magnification								
Magnification	105,000	105,000	105,000	105,000	105,000	105,000	105,000	105,000
Voltage (kV)	300	300	300	300	300	300	300	300
Electron exposure (e-/Å ²)	44	44	44	44	44	44	44	44
Defocus range (μm)	-0.6 to -3.5	-0.6 to -3.5	-0.6 to -3.5	-0.6 to -3.5	-0.6 to -3.5	-0.6 to -3.5	-0.6 to -3.5	-0.6 to -3.5
Pixel size (Å)	0.685	0.685	0.685	0.685	0.685	0.685	0.685	0.685
Symmetry imposed	C1	C1	C1	C1	C1	C1	C1	C1
Initial particle images (no.)	3,254,352	3,254,352	3,254,352	3,254,352	3,254,352	3,254,352	3,254,352	3,254,352
Final particle images (no.)	5,117	68,506	77,545	25,755	105,081	169,522	92,777	174,114
Map resolution (Å)	6.1	3.4	3.3	3.9	3.3	3.2	3.3	3.2
FSC threshold	0.143	0.143	0.143	0.143	0.143	0.143	0.143	0.143
Map resolution range (Å)	5.5-20.0	2.5-8.0	2.5-8.0	3.0-8.0	2.5-8.0	2.5-8.0	2.5-8.0	2.5-8.0
Refinement								
Initial model used	6MSG	6MSH	6MSH	6MSH	6MSH	6MSJ	6MSJ	6MSJ
Model resolution (Å)	3.4	3.8	4.3	4.1	4.0	3.9	3.8	3.8
FSC threshold	0.5	0.5	0.5	0.5	0.5	0.5	0.5	0.5
Model resolution range (Å)	3.2-8.0	3.1-8.0	3.7-8.0	3.1-8.0	3.0-8.0	3.1-8.0	3.0-8.0	3.0-8.0
Map sharpening <i>B</i> factor (Å ²)	-35	-35	-40	-35	-30	-35	-30	-30
Model composition								
Non-hydrogen atoms	105749	104415	103729	105343	105343	105343	105343	105343
Protein residues	13476	13314	13236	13488	13488	13488	13488	13488
Ligands	9	9	5	11	11	11	11	11
<i>B</i> factors (Å ²)								
Protein	174.88	178.15	167.88	213.61	211.63	148.64	165.65	
Ligand	143.96	106.39	268.45	208.40	183.93	154.06	175.01	
R.m.s. deviations								
Bond lengths (Å)	0.006	0.005	0.007	0.006	0.008	0.006	0.008	0.005
Bond angles (°)	1.017	0.888	0.980	1.079	1.115	1.027	0.987	0.893
Validation								
MolProbity score	1.83	1.65	1.73	2.44	2.47	2.28	2.45	2.45
Clashscore	5.57	4.17	4.39	18.24	18.78	16.38	18.97	17.86
Poor rotamers (%)	0.46	0.4	0.62	0.36	1.47	0.96	1.37	1.68
Ramachandran plot								
Favored (%)	90.89	91.88	91.97	89.47	89.31	89.58	89.09	90.79
Allowed (%)	8.77	7.91	7.82	10.17	10.32	10.1	10.78	8.99
Disallowed (%)	0.34	0.21	0.21	0.36	0.37	0.32	0.13	0.22

1503

1504

1505

1506

1507

1508

1509

1510 Cryo-EM data collection, refinement and validation statistics (continued)

	E _{D1.3}	E _{D2}	E _{D2.2}	E _{D2.3}	E _{A1.RPNI}	E _{D.a5}
Data collection and processing						
Magnification						
Magnification	105,000	105,000	105,000	105,000	105,000	105,000
Voltage (kV)	300	300	300	300	300	300
Electron exposure (e ⁻ /Å ²)	44	44	44	44	44	44
Defocus range (μm)	-0.6 to -3.5	-0.6 to -3.5	-0.6 to -3.5	-0.6 to -3.5	-0.6 to -3.5	-0.6 to -3.5
Pixel size (Å)	0.685	0.685	0.685	0.685	1.37	0.685
Symmetry imposed	C1	C1	C1	C1	C1	C1
Initial particle images (no.)	3,254,352	3,254,352	3,254,352	3,254,352	3,254,352	3,254,352
Final particle images (no.)	146,506	856,683	24,674	6,192	128,161	131,570
Map resolution (Å)	3.2	2.5	3.7	7.0	3.7	3.1
FSC threshold	0.143	0.143	0.143	0.143	0.143	0.143
Map resolution range (Å)	2.5-8.0	2.5-4.8	3.0-8.0	6.0-20.0	3.0-8.0	2.5-10.0
Refinement						
Initial model used	6MSJ	6MSK	6MSK		6MSK	6MSK
Model resolution (Å)	3.9	3.2	3.5		3.8	3.6
FSC threshold	0.5	0.5	0.5		0.5	0.5
Model resolution range (Å)	3.0-8.0	2.5-5.8	3.5-8.0		3.5-8.0	2.9-5.8
Map sharpening <i>B</i> factor (Å ²)	-30	-20	-40		-100	-25
Model composition						
Non-hydrogen atoms	63654	105218	107626	106422	7717	107626
Protein residues	8203	13420	13724	13572	994	13724
Ligands	11	11	11	11		11
<i>B</i> factors (Å ²)						
Protein	178.66	102.99	182.3		141.87	162.57
Ligand	187.12	116.74	162.17			135.00
R.m.s. deviations						
Bond lengths (Å)	0.005	0.004	0.005	0.005	0.005	0.007
Bond angles (°)	0.913	0.810	1.033	1.033	0.837	1.088
Validation						
MolProbity score	2.32	1.84	1.84	1.84	3.41	1.88
Clashscore	17.69	5.48	5.48	5.48	24.57	6.09
Poor rotamers (%)	0.47	0.69	0.69	0.69	12.01	0.73
Ramachandran plot						
Favored (%)	89.29	90.16	90.16	90.16	81.98	90.17
Allowed (%)	10.36	9.35	9.35	9.35	17.51	9.4
Disallowed (%)	0.34	0.49	0.49	0.49	0.51	0.43

1511